Steady-State Parallel Retreat Migration in River Bends with Noncohesive (Composite) Banks

David M. Waterman[1] and Marcelo H. García[2]

[1]Department of Civil and Environmental Engineering, South Dakota School of Mines and Technology, Rapid City, SD, USA, [2]Department of Civil and Environmental Engineering, University of Illinois at Urbana-Champaign, Urbana, IL, USA.

Corresponding author: David Waterman (David.Waterman@sdsmt.edu)

Key Points:

- Migration rate in the idealized case is dictated by transverse sediment flux at the thalweg due to secondary flow, not bank slope
- Migration rate is formulated from dimensionless groupings: excess Shields stress, depth/radius, and grain size/noncohesive layer thickness
- The linear excess shear stress formulation valid for cohesive soils mischaracterizes fluvial erosion when applied to noncohesive banks

Abstract

A substantial body of research has addressed the equilibrium cross-sectional geometry of straight noncohesive channels, along with bends having fixed outer banks. However, development of a characteristic cross-section during active migration has been confounded by inaccurate treatment of noncohesive bank erosion processes. This analysis characterizes a steady-state migrating cross-section and the associated migration rate for the highly conceptualized case of an infinite bend of constant centerline radius with noncohesive lower banks consisting of uniform-sized grains mobilized as bedload. Analytical, numerical, and field analyses are presented to rationally constrain the geometry and obtain a physically based migration rate equation dependent on the following dimensionless groupings: excess Shields stress, flow depth to radius of curvature ratio, and noncohesive bank thickness to grain size ratio. Migration rate is shown to be dictated by transverse sediment flux at the thalweg due to secondary flow, not bank slope as in previous formulations developed from similar principles. Simple outward translation can result without the characteristic cyclic process observed in cohesive banks (fluvial erosion, oversteepening, and mass failure). This suggests that the linear excess shear stress formulation that applies to cohesive soils misrepresents noncohesive bank erosion processes. A numerical model of cross-sectional evolution to steady-state migration is developed; when applied to the lower Mackinaw River in Illinois, it reveals that the river behaves as if the critical shear stress is considerably larger than that indicated by the grain size distribution. This conceptualized treatment is intended to provide a canonical basis of comparison for actual meander bend geometries.

Plain Language Summary

Meandering rivers erode their outer banks and deposit coarse-grained sand and gravel on the inside of bends. Finer-grained sediments (fine sand, silt, clay) deposit on top of the coarse-grained bar deposits. The fine-grained sediments generally are more cohesive and have increased strength and resistance to erosion. As the river migrates back and forth across its floodplain, the outer bank is commonly eroding into a bar deposit left behind by a former river configuration. This type of bank with a lower layer of sand and gravel and an upper layer of cohesive soil is known as a composite riverbank. River engineers need to predict migration rates to determine risk to infrastructure and to design measures to mitigate such risks. The equation used to model erosion of cohesive soils is mathematically simple. Largely because of the simplicity of the

cohesive sediment erosion rate equation, it has been used extensively to model the erosion of coarse-grained sand and gravel banks, even though the dominant physical factors governing the erosion are quite different than for cohesive soils. In this study, the characteristic shape and migration rate of a river with noncohesive banks is sought, using physical principles of sand/gravel erosion and deposition rather than the simplistic forms used for cohesive soils. A migration rate formulation is developed, and key aspects of the river cross-sectional shape are determined for an idealized case of a river bend migrating at steady state.

1 Introduction

1.1 Noncohesive bank deformation: state of the science summary

Bank soil composition is a primary factor that determines channel migration rates. Although few natural channels have banks consisting entirely of coarse-grained, noncohesive soil, a composite riverbank (Thorne & Tovey, 1981) is a common stratigraphy. A composite bank consists of a lower layer of noncohesive soil overlain by an upper layer of fine sand, silt, and clay. In the context of single-threaded meandering alluvial rivers, the lower layer is dominated by bed material sized sediment originally emplaced as lateral accretion deposits during migration of the stream across its floodplain. The upper layer consists of sediments primarily transported in suspension and deposited on bar tops and overbank areas, aided by vegetation establishment (e.g., Nanson, 1980; Tsujimoto, 1999). The primary mechanisms governing the erosion of composite riverbanks are fluvial erosion of the noncohesive basal material and associated geotechnical mass failure of the overlying material (Thorne & Tovey, 1981; Thorne, 1982). In the past several decades, these processes have been incorporated into a multitude of bank erosion models of varying sophistication; descriptions of relevant physical processes and many of the modeling approaches can be found in Rinaldi and Darby (2008) and Klavon et al. (2017).

Properly characterizing the fluvial erosion of noncohesive bank materials remains a weakness of morphodynamics models. This weakness exists despite substantial attention being given to the topic of noncohesive bank deformation during the 1980s and 1990s (e.g., Ikeda, 1981; Ikeda et al., 1988; Diplas, 1990; Pizzuto, 1990; Kovacs & Parker, 1994; Thorne et al., 1998). These studies characterized evolution of banks to a threshold channel configuration when a straight channel is subjected to excess boundary shear stress with the bank material mobilized as

bedload. The threshold channel concept (Glover & Florey, 1951), as modified by Parker (1978) to account for an active bedload transporting region, provided a coherent framework upon which bank deformation results could be generalized. Those studies that incorporated numerical modeling implemented several approaches to account for momentum extraction due to the transverse boundary layer associated with the bank; the resulting boundary shear stress distribution was then used to drive the boundary deformation due to transverse bedload flux divergence terms in the sediment mass conservation equation (Exner equation). Despite the success of these early modeling approaches, implementation of the numerical techniques developed for straight channels has been slow to be implemented into morphodynamics models for natural channels. This can be attributed primarily to the increased complexity of natural channel alignments and the consequent increased computational expense of accurately characterizing boundary shear stresses at a suitable spatial resolution, an issue highlighted by Rinaldi and Nardi (2013).

Presently, the most commonly used reach-scale modeling techniques that address fluvial erosion of basal noncohesive bank materials can generally be classified into two broad categories, which depend on the bank erosion modeling framework: (a) models that treat bank erosion through analysis of individual cross sections, in which the boundary shape and boundary shear stress distribution can be discretized at a denser spatial resolution than the width of the entire bank; and (b) spatially continuous two-dimensional (2D) morphodynamics models, in which the entire width of the bank at any longitudinal position along the stream may be comprised by few (or one) numerical cells.

With respect to the first category of bank erosion models, the most common method for fluvial erosion specifies the local fluvial erosion rate in the direction normal to the surface, E, as a linear function of the excess boundary shear stress:

$$E = k(|\boldsymbol{\tau_b}| - \tau_c) \tag{1}$$

where k is an erodibility coefficient, $\boldsymbol{\tau_b}$ is the boundary shear stress vector, and τ_c is the critical boundary shear stress. This linear formulation is also known as the Ariathurai-Partheniades equation (Ariathurai, 1974; McAnally & Mehta, 2001). The linear excess shear stress method is used in models such as BSTEM (Simon et al., 2000), CONCEPTS (Langendoen & Simon,

2008), and various physics-based models developed for academic research (e.g., Darby et al., 2007; Rinaldi et al., 2008). However, the formulation was developed based on experimental results using cohesive sediments. A recognized knowledge gap has been identified regarding suitable ways to specify the erodibility coefficient for noncohesive bank materials (e.g., Rinaldi et al., 2008; Rinaldi & Nardi, 2013). Rinaldi and Darby (2008) were compelled to assume that the equation is robust, given the lack of a suitable alternative, but they acknowledge that the physical basis of the equation is questionable. Waterman and García (2016) described how Eq. (1) is an entrainment rate equation that applies to sediments transported at less than the transport capacity of the flow, which improperly characterizes sediment mass conservation when dominated by noncohesive sediment transport. Nevertheless, the excess shear stress formulation continues to be extensively used in the cross-sectional models, primarily due to its ease of numerical implementation and long history of usage.

With respect to the second category of models, in which the bank region is discretized with few numerical cells, simplified conceptualizations of fluvial erosion and mass failure are generally "lumped" into algorithms of varying physical realism (Stecca et al., 2017). This lumped (or bulk) treatment is a practical necessity due to computational limitations with respect to modeling reach-scale spatially continuous domains. With this limitation in mind, the accurate expression of sub-grid scale bank processes as net bank retreat remains one of the major challenges of modern morphodynamics modeling (Siviglia & Crosato, 2016). The simplest of these lumped bank erosion models, which are not specific to either cohesive or noncohesive banks, specify the bulk bank retreat rate as a linear function of either the excess near-bank velocity or the excess near-bank boundary shear stress. Excess velocity refers to the difference between the near-bank velocity and the cross-sectional average velocity (Ikeda et al., 1981), while the excess shear stress refers to the difference between the boundary shear stress and a critical shear stress associated with the specific bank material. Mosselman (1998) explains that bulk bank erosion models based on excess shear stress conceptually represent a time-averaged description of parallel retreat (Osman and Thorne, 1988) that involves a cyclical sequence of basal fluvial erosion followed by large-scale mass failure. Numerous lumped noncohesive bank erosion algorithms of greater complexity are used in 2D morphodynamics models; the reader is referred to Stecca et al. (2017) for an enumeration and analysis of the most common ones.

One type of lumped algorithm not addressed in Stecca et al. (2017) is the integral treatment of the Exner equation applied over the bank region, which extends from the top of bank down to the thalweg, as originally formulated by Hasegawa (1989). Presumably, that method was not addressed in Stecca et al. (2017) because it is not widely used in 2D morphodynamics models. However, the bank-integrated method provides a theoretically sound basis for treating noncohesive soils. Hasegawa (1989) noted that the integral treatment mathematically formalized bank retreat principles described by Thorne (1982), in which the bank migration rate is driven by the balance between the supply of sediment from the bank to its base and the removal of that material, resulting in parallel retreat under conditions of unimpeded removal. The approach of Hasegawa (1989) was not exploited to its full advantage until more recently. Parker et al. (2011) described the mathematics of the integral treatment in greater detail and noted that simplified treatments yielding similar formulations were obtained and utilized by Duan et al. (2001) and Duan and Julien (2005). Since the work of Parker et al. (2011), the bank-integrated approach has been utilized by Asahi et al. (2013) and Eke et al. (2014), among others. The bank-integrated Exner equation is further explored in this paper as a robust physics-based method to treat fluvial erosion of noncohesive bank materials in bulk bank erosion models.

1.2 Motivation, Objectives, and Approach

Substantial research on composite riverbank migration in recent years has focused on channel migration rates being influenced by differential rates of outer bank erosion and inner bank accretion (e.g., Parker et al., 2011; Eke et al., 2014) and on slump block armoring of the noncohesive bank layer (e.g., Parker et al., 2011; Motta et al., 2014; Hackney et al., 2015). However, more fundamental questions remain unanswered. For example, if the inner bank and outer bank were to migrate at equal rates (constant-width migration), what would be the expected cross-sectional shape of the channel, particularly in the bank region? Similarly, if bank armoring were not present, what would be the bank shape and the migration rate? The present analysis is motivated by these questions, with the intention that the answers will both improve fundamental understanding of noncohesive bank migration and yield useful results for modeling.

The bank-integrated Exner equation approach for bank migration requires calculation of the transverse flux of sediment from the base of the bank region, which is dependent on both the

effects of secondary flow and gravity due to bank slope on bedload movement. The integral treatment as implemented by Hasegawa (1989) and Parker et al. (2011) requires a similarity function for the cross-sectional shape of the bank. In those analyses, the bank shape was assumed to have a uniform transverse slope; however, a rational physically-based manner of specifying the bank shape *a priori* has never been established. Thus, the first objective of the analysis is to suitably constrain the bank shape for use in the integral treatment. The second objective is to utilize the shape constraint to express the bank-integrated Exner equation for migration rate in a suitable form for implementation in numerical models of rivers having noncohesive or composite banks. The third objective is to demonstrate numerically that parallel retreat as conceived in the analytical treatment as a simple outward translation of the cross-section (not the cyclic process of fluvial erosion, oversteepening, and mass failure) is feasible in noncohesive bank materials.

Simplification is required to satisfy the objectives and elucidate the essential aspects of noncohesive bank deformation in meandering rivers. The following simplifications are implemented in the current analysis: (a) fully-developed flow in a constant radius bend of low to moderate curvature based on the nomenclature of Blanckaert (2011); (b) uniform-sized sediment mobilized only as bedload; (c) the fine-grained upper layer plays no role in the bank migration dynamics, e.g., through armoring of the noncohesive layer. The cross-sectional shape is sought that migrates without changing shape (parallel retreat) under a constant discharge. The simplified analysis indicates a tendency toward which channel geometry can be expected to adjust for a given discharge and provides the canonical case for evaluating deviations from the idealized conditions. More physically realistic representations of all the complexities of natural channels can be developed in the future once the simplest condition is better understood.

The paper is organized as follows. In Section 2, the integrated Exner equation is explored to identify the conditions required to achieve parallel retreat and to establish the basic form of the migration rate equation whose terms must be quantified. Section 3 theoretically establishes the parallel retreat shape constraint of zero transverse slope (horizontal) at the channel thalweg; this is contrasted with the implied similarity functions of Hasegawa (1989) and Parker et al. (2011). The new shape constraint allows further quantification of terms in the migration rate equation, which is then expressed in dimensionless form as a function of the excess Shields stress. In Section 4, a simplified numerical model is presented to demonstrate that parallel retreat as simple

translation is feasible in noncohesive materials as conceived in the theoretical analysis. In Section 5, the numerical model is applied to a bend of the Mackinaw River, and the simulation parameters that yield results that best represent the field observations are described. Finally, in Section 6 organizing principles are discussed that provide a coherent framework upon which noncohesive bank deformation can be generalized across both straight and meandering reaches; the results are also discussed in terms of relating the highly simplified conceptual model to the complexities of real rivers.

2 Mathematical and Physical Bases of Parallel Retreat

2.1 Integrated Exner Equation and Assumptions

The infinite bend configuration (fully-developed flow, constant centerline radius) used throughout this analysis is illustrated in Figure 1. The governing equations are most conveniently expressed in modified cylindrical coordinates (s, r, z), where s is the streamwise coordinate, r is the radial coordinate, and z is the vertical coordinate. The modified cylindrical coordinates are converted to standard cylindrical coordinates based on the relationship $s = r\theta$, where θ is the angle turned about the center point in a plane where z = constant. The longitudinal slope of the channel is considered small, such that (s, r, z) are orthogonal coordinates. The variables r_{in}, r_c, and r_{out} represent the radii of the inner boundary, the centerline, and the outer boundary of the channel, respectively. The radial position of the center point of the circle is denoted r_{cp}, which always equals 0.

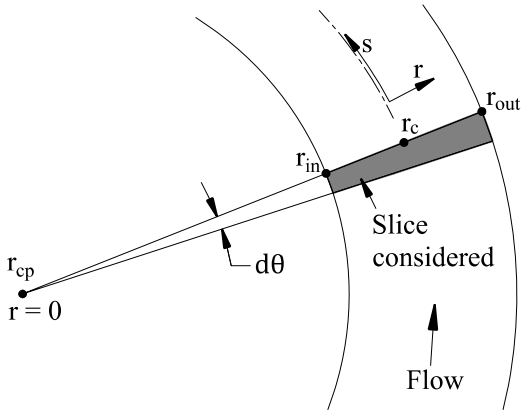

Figure 1: Plan view showing radial slice considered in analysis

The constant migration rate M is sought for a channel geometry that does not change during migration under a steady bankfull discharge Q_{bf}. To maintain constant radial values as the channel migrates, the (s, r, z) coordinate system must represent a translating frame of reference rather than concentric expansion on a fixed frame of reference. The resulting governing equations have the same basic structure as the more commonly used intrinsic (s, n, z) coordinate system (e.g., Parker et al., 2011) where the origin of the transverse n coordinate is associated with the dynamic channel centerline. In Figure 2, the translating frame of reference is illustrated with respect to a fixed frame of reference, in which the radial coordinate for the latter is denoted with R. For each value r_{cp}, r_{in}, r_c, and r_{out} in the translating system, an associated value R_{cp}, R_{in}, R_c, and R_{out}, respectively, exists in the fixed frame of reference.

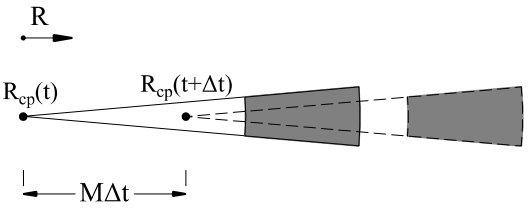

Figure 2: Plan view showing translated radial slice on a fixed coordinate system after a long time interval Δt

In Fig. 2, the shaded region represents the channel and t represents time. The following relations describe the time-invariant radial quantities under the constant migration rate M.

$$\frac{dr_{in}}{dt} = \frac{dr_c}{dt} = \frac{dr_{out}}{dt} = 0 \tag{2}$$

$$\frac{\partial r_{in}}{\partial t} = \frac{\partial r_c}{\partial t} = \frac{\partial r_{out}}{\partial t} = M \tag{3}$$

The above relations are ensured through evaluating the total derivative, with the following expressions being valid for any of the r terms:

$$r = R - R_{cp} \tag{4}$$

$$\frac{dr}{dt} = \frac{\partial r}{\partial t} + \frac{\partial r}{\partial R_{cp}}\frac{dR_{cp}}{dt} \tag{5}$$

where dR_{cp}/dt is the migration rate M and $\partial r/\partial R_{cp}$ is -1 from Eq. (4). The constant channel width B is expressed as $B = r_{out} - r_{in}$. The steady discharge Q_{bf} is entirely conveyed between r_{in} and r_{out}.

The volumetric bedload transport rate per unit width vector, $\boldsymbol{q}$, is decomposed into a streamwise component, q_s, and a transverse component tangent to the boundary surface in the r-z plane, q_{rt}. In modified cylindrical coordinates, the Exner equation is expressed as:

$$\frac{\partial \eta}{\partial t} = -\frac{1}{(1-\lambda)}\left[\frac{\partial q_s}{\partial s} + \frac{\partial q_{rt}}{\partial r} + \frac{q_{rt}}{r}\right] \tag{6}$$

where η represents the surface elevation above an arbitrary vertical datum, and λ is the porosity of the granular medium. The partial derivative of q_{rt} is taken with respect to the coordinate r rather than a boundary-fitted coordinate defined tangent to the surface in the r-z plane, as derived in Waterman and García (2016). In steady, uniform bend flow, the divergence terms in the s-direction vanish, allowing simplification to:

$$\frac{\partial \eta}{\partial t} = -\frac{1}{(1-\lambda)}\left[\frac{\partial q_{rt}}{\partial r} + \frac{q_{rt}}{r}\right] \tag{7}$$

Utilizing the definition of the total derivative of $\eta(t,r)$ yields the following:

$$\frac{d\eta}{dt} = \frac{\partial \eta}{\partial t} + \frac{\partial \eta}{\partial r}\frac{\partial r}{\partial t} \tag{8}$$

For parallel migration, in which the shape does not change within the translating frame of reference, $\mathrm{d}\eta/\mathrm{d}t = 0$. This treatment presupposes that the parallel retreat process is not a time-averaged depiction of a cyclical process of basal erosion and mass failure in the bank region, but rather a simple translation of the entire cross section due to local erosion and deposition. Substituting from Eq. (3), Eq. (8) is re-expressed accordingly:

$$\frac{\partial \eta}{\partial t} = -M\frac{\partial \eta}{\partial r} \tag{9}$$

Eq. (9) ensures that the bank region is erosional when considered on a fixed frame of reference due to $\partial\eta/\partial r$ being positive. Substituting Eq. (9) into Eq. (7) yields:

$$M(1-\lambda)\frac{\partial \eta}{\partial r} = \frac{\partial q_{rt}}{\partial r} + \frac{q_{rt}}{r} \tag{10}$$

Following the technique of Hasegawa (1989) and Parker et al. (2011), Eq. (10) is integrated in the radial direction; the limits of integration can be set at any arbitrary r positions on the cross-section. Integrating over the r-direction between arbitrary radial positions r_A and r_B yields:

$$M(1-\lambda)\left(\eta|_{r_B}-\eta|_{r_A}\right)=q_{rt}|_{r_B}-q_{rt}|_{r_A}+\int_{r_A}^{r_B}\frac{q_{rt}}{r}dr \tag{11}$$

$$M=\frac{q_{rt}|_{r_B}-q_{rt}|_{r_A}+\int_{r_A}^{r_B}\frac{q_{rt}}{r}dr}{(1-\lambda)\left(\eta|_{r_B}-\eta|_{r_A}\right)} \tag{12}$$

Note that the same result is obtained by integrating Eq. (7) over the r direction and implementing the Leibniz integral rule, which was the technique used by Parker et al. (2011). Ultimately, Eq. (12) will be used to formulate the migration rate; a key aspect of the analysis is to appropriately establish the positions r_A and r_B where q_{rt} and η can be readily quantified.

2.2 Boundary Conditions and their Implications

The boundary condition is imposed that $q_{rt}|_{r_{out}} = 0$; i.e., no bedload enters the domain from the cohesive upper layer as the channel migrates. Under the idealized condition, the upper cohesive layer passively fails as the noncohesive layer migrates, and that material is carried away in suspension. The boundary condition is also imposed that $q_{rt}|_{r_{in}} = 0$. The basis of the latter boundary condition is that, by problem definition, no discharge is conveyed where $r < r_{in}$. Thus, the mean flow velocity, bed shear stress, and bedload transport rate at the boundary are equal to zero. The conceptual interface at $r = r_{in}$ is illustrated in Fig. 3; the flow depth is non-zero at the interface, but dense vegetation in the region $r < r_{in}$ is presumed to maintain negligible velocity. The necessity of the non-zero flow depth at the inner boundary is described later in this section. The circled numbers in Fig. 3 indicate the following characteristics of the regions that form the channel boundary and just beyond it: (1) cohesive upper layer; (2) noncohesive lower layer; (3) vegetated over-bar area that is submerged under moderate and high flow conditions. Fig. 3 shows that $\eta|_{r_{in}}$ and $\eta|_{r_{out}}$ are elevations associated with the noncohesive layer and r_{thal} is the radial coordinate of the thalweg. Fig. 4 illustrates regions of aggradation (net deposition) and degradation (net erosion) that must exist in a fixed spatial frame of reference under conditions of parallel retreat. The shape of the cross-section in Figs. 3 and 4 is not imposed; the only shape assumption made is that $\partial\eta/\partial r \leq 0$ throughout the region left of the thalweg and $\partial\eta/\partial r \geq 0$

throughout the region right of the thalweg. The cross-sectional shape illustrated in the figures is only provided to aid the description of the problem setup.

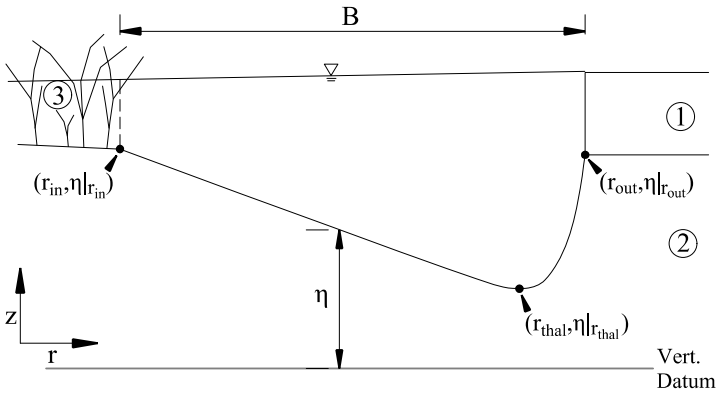

Figure 3: Cross-sectional view showing radial slice considered in analysis

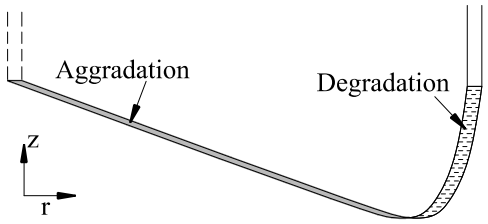

Figure 4: Cross-sectional view showing the translating section on a fixed spatial frame of reference at two instants in time

With the shape assumption that $\partial\eta/\partial r \leq 0$ throughout the region left of the thalweg, the outermost location of maximum η must be aggradational and emplaced as the channel migrates. Since aggradation necessitates the condition that $\partial q_{rt}/\partial r \neq 0$, the flow must be competent to transport bedload infinitesimally close to the location of maximum η. This establishes the non-zero flow depth requirement at the inner boundary illustrated in Fig. 3.

The $q_{rt}|_{r_{out}} = q_{rt}|_{r_{in}} = 0$ boundary conditions also have implications on the elevation of $\eta|_{r_{in}}$ relative to $\eta|_{r_{out}}$. To achieve parallel migration, the volume of noncohesive sediment eroded must be exactly balanced by the volume deposited in the fixed frame of reference. However, the eroded sediment originates from the region where a control volume has a relatively large dimension in the *s*-direction, while sediment deposits in the region where a control volume has a smaller *s*-direction dimension (see Fig. 1). Thus, to achieve the volume balance, deposited sediment must reach a somewhat higher elevation at the inner edge than the elevation of eroded material at the outer edge to compensate for the control volume shape. The mathematical demonstration of this

assertion is provided in Appendix A. This requires that $\eta|_{r_{out}}$ cannot be arbitrarily high on the outer bank but must be lower than the elevation at which bedload can be transported at the inner bank.

3 Rational Shape Constraint and Resulting Migration Rate Equation

3.1 Development of the Shape Constraint

The key to using Eq. (12) is appropriately establishing the positions r_A and r_B where q_{rt} and η can be readily quantified. At the outer boundary, $q_{rt} = 0$, and $\eta|_{r_{out}}$ can be estimated with respect to the top of bank using a typical depth of the cohesive top layer. Therefore, r_{out} is the most straight-forward choice for setting r_B in Eq. (12). Selecting the position r_A is more challenging, as q_{rt} is a function of the covarying hydrodynamics and boundary shape, which are not known *a priori*. A rational shape constraint to generalize the calculation of q_{rt} at a specific location r_A is therefore sought. Figure 5 is a definition diagram showing variables required for the bedload transport rate evaluation, and previously undefined variables shown are described after the figure.

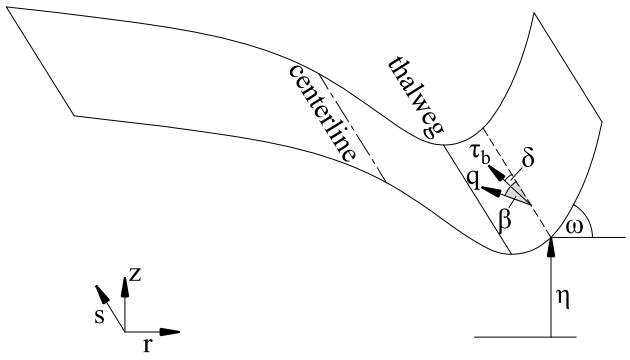

Figure 5: Oblique view of channel illustrating several angles used in the bedload transport calculations

On Fig. 5, the variable δ is the deviation angle of $\boldsymbol{\tau_b}$ relative to the s-direction, with the positive direction always toward the outer bank; β is the deviation angle of $\boldsymbol{q}$ relative to the s-direction, with the positive direction always toward the outer bank; and ω is the boundary inclination angle, defined according to:

$$\tan\omega = \frac{\partial\eta}{\partial r} \tag{13}$$

The calculation of q_{rt} requires Eqs. (14) through (20):

$$\tau_c = K_B \tau_{c0} \tag{14}$$

$$K_B = \frac{\sin\omega \sin\delta}{\mu_s} + \sqrt{\left(\frac{\sin\omega \sin\delta}{\mu_s}\right)^2 - \left(\frac{\sin\omega}{\mu_s}\right)^2 + \cos^2\omega} \tag{15}$$

$$\mu_s = \tan\theta_{rp} \tag{16}$$

where K_B is the dimensionless Brooks coefficient (Brooks & Shukry, 1963); τ_{c0} is the critical shear stress on a horizontal bed; μ_s is the static friction coefficient; and θ_{rp} is the particle angle of repose (Wiberg and Smith, 1987). A summary of the derivation of K_B is provided in Vanoni (1975). When using the assumption of transverse slope only (longitudinal slope negligible), the relation of Kovacs and Parker (1994; Eq. 18 therein) is identical to the above formulation. When $\delta = 0$, K_B is equivalent to the more commonly known expression from Lane (1955; Eq. 1 therein). The bedload transport rate vector magnitude is calculated according to:

$$|\boldsymbol{q}^*| \equiv \frac{|\boldsymbol{q}|}{\sqrt{gR_sD_{50}}D_{50}} = \begin{cases} K_0(|\boldsymbol{\tau}^*| - \tau_c^*)^{1.5} & \text{for } |\boldsymbol{\tau}^*| > \tau_c^* \\ 0 & \text{for } |\boldsymbol{\tau}^*| \le \tau_c^* \end{cases} \tag{17}$$

$$\boldsymbol{\tau}^* \equiv \frac{\boldsymbol{\tau_b}}{\rho g R_s D_{50}} \tag{18}$$

where $\boldsymbol{q}^*$ is the dimensionless volumetric bedload transport rate per unit width; g is the gravitational acceleration constant; R_s is the sediment submerged specific gravity; D_{50} is the median sediment grain size, which in the present analysis is the specified uniform grain size; K_0 is an empirical constant, which equals 5.7 in Fernandez-Luque and van Beek (1976); $\boldsymbol{\tau}^*$ is the Shields number; and τ^*_c is τ_c made dimensionless using Eq. (18). The bedload transport rate vector direction is calculated according to:

$$\tan\beta \equiv \frac{q_{rt}}{q_s} = \tan\delta - A\left(\frac{\tau_{c0}^*}{|\boldsymbol{\tau}^*|}\right)^{0.5} \tan\omega \tag{19}$$

where A is a coefficient that is assumed constant in linear formulations (e.g., Parker, 1984) and has dependence on β, ω and δ in nonlinear formulations that account for steep slopes (Waterman & García, 2019). Following calculation of $|\boldsymbol{q}^*|$ and β, q_{rt} is calculated as:

$$q_{rt} = |\boldsymbol{q}^*|\sqrt{gR_sD_{50}}D_{50}\sin\beta = |\boldsymbol{q}^*|\sqrt{gR_sD_{50}}D_{50}\frac{\tan\beta}{(1+\tan^2\beta)^{0.5}} \tag{20}$$

Direct calculation of q_{rt} is possible if values for $\boldsymbol{\tau_b}$ (both magnitude and direction) and ω are known, which highlights the importance of being able to specify ω at the location where r_A will be chosen. In previous analyses, Hasegawa (1989) and Parker et al. (2011) specified ω as a constant value over the entire bank and set the position r_A for usage in their integral formulations to the thalweg position; i.e., the inner boundary of the bank region. The thalweg is the most logical location for r_A, as it is a nonarbitrary feature that can be identified on any cross-section. However, the value of ω should not be assigned arbitrarily, as it clearly influences q_{rt}, through both τ_c (Eqs. 14 and 15) and β (Eq. 19). Further reinforcing this point, Hasegawa (1989) considered the tanω term in Eq. (19) to be the primary driver in the decomposition of $\boldsymbol{q}$; more specifically, he neglected the tanδ term in Eq. (19) as being of a lower order of magnitude than the tanω term. This analysis reexamines that assumption by analytically establishing the value of ω at the thalweg.

The characteristic cross-section of Parker et al. (2011; Fig. 10 therein) is provided as Fig. 6 below, as that cross-section is directly contrasted with an alternative shape constraint developed for the thalweg in the present analysis. Note that the Parker et al. (2011) cross-section was specifically intended not to be a parallel retreat cross-section, as it allowed the region bankward of the thalweg and barward of the thalweg to adjust independently.

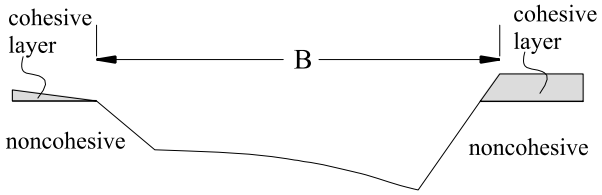

Figure 6: The characteristic cross-section of Parker et al. (2011; Fig. 10 therein)

As the thalweg is defined as the position of minimum η on the cross-section, $\partial\eta/\partial r$ would equal zero if the function of η versus r was a continuous, differentiable function; thus, ω would equal zero. However, it is not evident that η versus r is necessarily a continuous, differentiable function; the abrupt grade-break at the thalweg in the Parker et al. (2011) cross-section is the alternative. Two different conditions may prevail at a potential grade-break: first is that in which q_{rt} varies continuously and smoothly with respect to r; second is that in which an abrupt discontinuity in the relationship between q_{rt} and r exists at the thalweg, referred to as a shock in

Parker et al. (2011). In the first scenario, an abrupt topographic break is not possible. Continuous variation of q_{rt} with respect to r requires that $q_{rt}|_{r_{thal}}$, calculated from both ω values bounding the thalweg, be equal. For clarity, these ω values are referred to as ω_{left} and ω_{right}. To ensure sediment is evacuated from the bank region for a migrating cross-section, this $q_{rt}|_{r_{thal}}$ value must be negative. Although ω may have multiple values at a point in space, as in the case of the grade-break, $\boldsymbol{\tau}^*$ must be single-valued at a point in space on physical grounds. As helical flow causes $\boldsymbol{\tau}^*$ to be directed inward (to the left, negative δ) at a bend, bedload left of the thalweg is driven upslope, and bedload right of the thalweg is driven downslope; intuitively, q_{rt} should be more negative when comparing any ω_{right} to ω_{left}, and this is indeed the case, based on the following considerations. Noting that $q_{rt}|_{r_{thal}}$ equals $|\boldsymbol{q}|\sin\beta$, the transverse slope influences both $|\boldsymbol{q}|$ and β. Right of the thalweg, an increase in inclination tends to increase $|\boldsymbol{q}|$ through a decrease in τ^*_c (Eqs. 14 and 15); while an increase in inclination makes β more negative (Eq. 19). Thus, q_{rt} monotonically becomes more negative with increased inclination. Left of the thalweg, the situation is more complex. An increase in inclination causes β to become more positive (Eq. 19), but $|\boldsymbol{q}|$ does not monotonically increase or decrease; Eqs. (14) and (15) indicate that with increased inclination τ^*_c initially increases to a maximum greater than τ^*_{c0} and then decreases. While a mathematically elegant solution was not obtained to demonstrate that $q_{rt}|_{r_{thal}}$ cannot be the same for different values of ω under the specific conditions evaluated, the following expression obtained from Eqs. (14) through (20) is used for the demonstration:

$$\frac{[q_{rt}]_{left}}{[q_{rt}]_{right}} = \frac{\left[\left(|\boldsymbol{\tau}^*|-K_B\tau^*_{c0}\right)^{1.5}\tan\beta/\left(1+\tan^2\beta\right)^{0.5}\right]_{left}}{\left[\left(|\boldsymbol{\tau}^*|-K_B\tau^*_{c0}\right)^{1.5}\tan\beta/\left(1+\tan^2\beta\right)^{0.5}\right]_{right}} \tag{21}$$

The variables K_B and β are each a function of ω and δ, which are calculated from Eqs. (15) and (19), respectively; $|\boldsymbol{\tau}^*|$ and δ are treated as parameters and are evaluated across a reasonable parameter space based on gravel-bed streams. The variable ω_{right} is set to 0, which yields the least negative value of $q_{rt}|_{r_{thal}}$ that can be obtained for ω_{right}. For each combination of $|\boldsymbol{\tau}^*|$ and δ evaluated, ω_{left} is evaluated over the entire range from 0 to -40 degrees at 1-degree intervals to find the maximum value of the ratio; a ratio of 1 for any $\omega_{left} < 0$ indicates the grade-break is possible. The value of $|\boldsymbol{\tau}^*|$ is varied from 0.046 to 0.20 in intervals of 0.002; and δ is varied from -1 to -45 degrees in 1-degree intervals. All combinations of these parameters are evaluated. Constants used in the analysis are $\mu_s = 0.84$; $A = 1.54$; $\tau^*_{c0} = 0.045$. The results reveal that the

maximum value of the ratio in Eq. (21) is uniformly 1.0 for all combinations, associated with $\omega_{left} = 0$. Therefore, any $\omega_{right} > 0$ (resulting in a more negative q_{rt}) will not yield a solution; and the only solution is:

$$\omega_{left} = \omega_{right} = 0 \tag{22}$$

$$\omega|_{r_{thal}} = 0 \tag{23}$$

In other words, the grade-break is not permissible for this first scenario that does not include a shock condition. A potential complicating factor to the above analysis is whether the parameter A in Eq. (21) is properly treated as a constant. For transverse slopes up to approximately 10° relative to horizontal, this linear assumption includes minimal error compared to a more robust nonlinear formulation of A, such as that derived in Waterman and García (2019), which was based on Kovacs and Parker (1994) and Seminara et al. (2002). The nonlinear expression of A in Waterman and García (2019) is the following:

$$A = \chi \frac{1}{(\mu_S \mu_D)^{0.5}} \left(\frac{\cos\omega\left(1+\tan^2\delta\right)}{\cos\beta\left(1+\left(\tan\beta+\frac{\tan\omega}{\mu_D\cos\beta}\right)^2\right)^{0.5}} \right)^{0.5} \tag{24}$$

where χ is a dimensionless coefficient that expresses the ratio between the mean fluid velocity impinging on a static particle versus a particle moving in the bedload layer; and μ_D is the dynamic friction coefficient. Solving β in Eq. (19) iteratively using the expression from Eq. (24) for A, the same process of evaluating Eq. (21) over the same parameter space is repeated. The results are identical; the maximum value of the ratio is 1.0 across the entire space, associated with $\omega_{left} = 0$.

The second scenario in which the grade-break may exist is that associated with an abrupt discontinuity in the q_{rt} versus r relationship. Under this shock condition, the only constraints to $q_{rt}|_{r_{thal}}$ values associated ω_{left} and ω_{right} are that the two $q_{rt}|_{r_{thal}}$ be negative to ensure sediment evacuation from the bank region; and the integral condition (Eq. 12) must have the same solution for both the region bankward of the thalweg (in which $r_A = r_{thal}$ and $r_B = r_{out}$) and inward of the thalweg (in which $r_A = r_{in}$ and $r_B = r_{thal}$). With only these constraints, the potential presence of a

grade-break cannot be disproven mathematically. Nevertheless, through physical reasoning, some approximate conclusions can be drawn. The $\boldsymbol{\tau_b}$ distribution in the vicinity of the grade-break is effectively that which exists at the corner of a trapezoidal channel. The $\boldsymbol{\tau_b}$ increases bankward of such a corner for a short distance, reaching its maximum value a short distance up the bank (e.g., Thorne et al., 1998; Khodashenas & Paquier, 1999), depending on the corner angle. Without any consideration of the region interior to the thalweg, for such a situation to exist under parallel retreat, Eq. (9) requires that the outer bank must be erosional across its entirety; and Eq. (7) requires that $\partial q_{rt}/\partial r$ be positive over its entirety to counteract the effect of the negative q_{rt}/r and ensure erosion. However, in the near-corner region, q_{rt} would be more negative moving outward ($\partial q_{rt}/\partial r$ negative) where $\boldsymbol{\tau_b}$ increases up a slope of constant or increasing ω. This violates the requirement of Eq. (9); during bank profile evolution, the near-corner region will be depositional according to Eq. (7), thus tending to smooth out the discontinuity. This always occurs in the development of straight channel experiments in uniform noncohesive materials (e.g., Ikeda, 1981), and also for the few documented cross-section sets in noncohesive experimental meandering channels (e.g., Friedkin, 1945; Schumm and Khan, 1972), even though these latter cannot be presumed to constitute equilibrium parallel retreat cross-sections. While this does not rise to the level of mathematical proof, it does suggest that the formation of a grade-break is unlikely under the assumptions of this analysis, and the most justifiable shape constraint is the one developed previously, namely that $\omega|_{r_{thal}} = 0$.

3.2 Migration Rate Equation

The migration rate formulation is preferably expressed in terms of either excess shear stress or excess velocity to maintain convention and provide a more direct comparison with past formulations. The $\omega|_{r_{thal}} = 0$ shape constraint has convenient consequences with respect to implementation in Eq. (12) when setting r_A to r_{thal}. First, according to Eqs. (14) and (15), $\tau_c = \tau_{c0}$. Second, according to Eq. (19), $\tan\beta = \tan\delta$. Third, with $\omega = 0$, simple formulations for the bedload transport vector magnitude (Eq. 17) contain no error associated with the effect of steep slopes. These three factors lead to simplifications in developing Eq. (12) into the form of an excess shear stress equation. Setting the positions $r_A = r_{thal}$ and $r_B = r_{out}$ in Eq. (12), with the boundary condition that $q_{rt}|_{r_{out}} = 0$, yields the following equation:

458 $$M = \frac{-q_{rt}|_{r_{thal}} + \int_{r_{thal}}^{r_{out}} \frac{q_{rt}}{r} dr}{(1-\lambda)\left(\eta|_{r_{out}} - \eta|_{r_{thal}}\right)} \quad (25)$$

459 Since the shape constraint does not fully specify the channel geometry through a similarity
460 function, various terms must be left in the formulation as parameters to be specified or neglected
461 on order-of-magnitude considerations until future advances are achieved. Of primary concern are
462 the following: (1) $\eta|_{r_{thal}}$; (2) the transverse proximity of r_{thal} to r_{out}, which determines the
463 momentum extraction due to the side-wall effects, and consequently directly affects $q_{rt}|_{r_{thal}}$; and
464 (3) the integral term in the numerator that results from the varying shape of the control volume in
465 the radial direction. The latter term can be neglected on order-of-magnitude considerations,
466 based on the following factors. At the thalweg, $\tan\beta = \tan\delta$ and the near-bed flow is toward the
467 inside of the bend (e.g., Rozovskii, 1961); thus, $\tan\beta$, $\tan\delta$, and q_{rt} are negative at r_{thal}. This
468 requires that q_{rt} transition from the negative value at r_{thal} to zero at r_{out}. Eq. (10) indicates that
469 where $\partial\eta/\partial r=0$, then $\partial q_{rt}/\partial r \approx 0$; i.e., it is near a local minimum in q_{rt} versus r. When making the
470 conservative assumption that the large negative q_{rt} value that prevails at the thalweg is constant
471 over the integral limits, the integral is still smaller than the first term in the numerator by a factor
472 of $\ln(r_{out}/r_{thal})$. This logarithm will generally be less than 0.1 ($r_{out}/r_{thal} < 1.1$), given that the width
473 of the bank region is generally much smaller than the thalweg radius.

474 To further refine Eq. (25), $\boldsymbol{q}$ must be obtained through hydrodynamic analysis and then
475 decomposed to express $q_{rt}|_{r_{thal}}$. For the case of steady, uniform bend flow, the s-momentum
476 equation for a thin control volume encompassing the full flow depth can be expressed in the
477 following alternative forms upon neglecting the cross-stream and vertical transport of s-
478 momentum:

479 $$\tau_{b,s} = c_0 \rho g h S \quad (26a)$$

480 $$\tau_{b,s} = \rho g h' S \quad (26b)$$

481 where $\tau_{b,s}$ is the s-component of $\boldsymbol{\tau_b}$. Eq. (26a) is based on a thin control volume with vertical
482 edges in which c_0 is a dimensionless coefficient between 0 and 1 (e.g., Ikeda & Nishimura, 1986)
483 that accounts for momentum extraction due to fluid shear stress on the transverse face associated
484 with the bank; h is the local flow depth; and S is the local longitudinal slope. Eq. (26b) is based

485 on an irregular-shaped control volume configured such that the *s*-directed fluid shear stresses on
486 the transverse faces equal 0 (e.g., Pizzuto, 1990). In this configuration, *h'* is the local hydraulic
487 radius, which is the cross-sectional area of the irregular control volume divided by its wetted
488 perimeter. From Eqs. (26a) and (26b):

489 $$h' \equiv c_0 h \tag{27}$$

490 The transverse component of $\boldsymbol{\tau_b}$ for steady, uniform bend flow can be calculated based on the
491 analytical treatments of van Bendegom (1947), Rozovskii (1961), and others, which take the
492 form:

493 $$\tan\delta \equiv \frac{\tau_{b,rt}}{\tau_{b,s}} = -K_1 \frac{h'}{r} = -K_1 c_0 \frac{h}{r} \tag{28}$$

494 where $\tau_{b,rt}$ is the transverse component of $\boldsymbol{\tau_b}$ tangent to the plane of the surface; and K_1 is an order
495 10 dimensionless constant taking values between 7 (Engelund, 1974) and 11 (Rozovskii, 1961).
496 The theoretical analyses that established Eq. (28) were based on integration over a vertical slice
497 of the stream unaffected by the fluid shear stress associated with the side walls. As a result, van
498 Bendegom (1947) and Rozovskii (1961) obtained the local flow depth (*h*) rather than *h'* in the
499 numerator of Eq. (28). However, when integrating the centripetal acceleration, the radial pressure
500 gradient, and the boundary shear stress following van Bendegom (1947) over an irregular control
501 volume configured to eliminate shear stress on the transverse faces, the variable that results is *h'*,
502 which is equivalent to *h* when the control volume is a vertical slice unaffected by side walls. The
503 resultant boundary shear stress is used to calculate the bedload transport rate:

504 $$|\boldsymbol{\tau_b}| = \gamma \tau_{b,s} \tag{29}$$

505 $$\gamma \equiv (1 + \tan^2\delta)^{0.5} \tag{30}$$

506 where γ is defined to make subsequent equations more concise. The following conditions prevail
507 at the thalweg: $\omega = 0$; $\tan\beta = \tan\delta$; and $\tau_c = \tau_{c,0}$. An expression for $q_{rt}|_{r_{thal}}$ is obtained using Eqs.
508 (17) through (20) and Eq. (28):

509 $$q_{rt}|_{r_{thal}} = \left(-\frac{c_0 K_0 K_1}{\gamma}\left(\gamma\tau^*_{b,s} - \tau^*_{c0}\right)^{1.5}\sqrt{gR_s D_{50}} D_{50}\frac{h}{r}\right)\Big|_{r_{thal}} \tag{31}$$

Note that if $\gamma = 1$ is specified, this is equivalent to the simpler, but less rigorous, approach of calculating q_s directly from $\tau_{b,s}$ rather than from $|\boldsymbol{\tau_b}|$. Substituting Eq. (31) into Eq. (25) leads to a dimensionless migration rate equation that is in the form of an excess Shields stress formulation:

$$M^* \equiv \frac{M}{\sqrt{gR_sD_{50}}} = \begin{cases} \left(\frac{c_0K_0K_1}{\gamma(1-\lambda)}\frac{D_{50}}{H_{nc}}\frac{h}{r}(\gamma\tau_s^* - \tau_{c0}^*)^{1.5}\right)\Big|_{r_{thal}} & \text{for } \gamma\tau_s^* > \tau_{c0}^* \\ 0 & \text{for } \gamma\tau_s^* \leq \tau_{c0}^* \end{cases} \tag{32}$$

$$H_{nc} \equiv \left(\eta|_{r_{out}} - \eta|_{r_{thal}}\right) \tag{33}$$

where M^* is the dimensionless migration rate; H_{nc} is the thickness of the noncohesive layer with respect to the deepest point in the channel; and τ^*_s is $\tau_{b,s}$ made dimensionless using Eq. (18). Although additional terms such as τ^*_s and γ can be more fully expressed in terms of h and r, the form of Eq. (32) is preferred, as it more directly expresses the migration rate dependence in terms of the following dimensionless groupings: (D_{50}/H_{nc}), (h/r), and τ^*_s. Note that when $h/r = 0$ (straight channel), $M = 0$, as the steady state is simply the threshold channel that can contain a region of active bedload transport at the thalweg.

4 Numerical Model

4.1 Overview

A simplified numerical model is presented to answer several questions that the analytical treatment cannot: (1) Is parallel retreat possible without incorporating a time-averaged cyclical process of basal erosion and mass failure within the noncohesive layer? (2) What is the resulting channel shape ($\eta|_{r_{thal}}$, r_{thal}, etc.)? The first question naturally arises due to long-held misconceptions regarding the nature of fluvial erosion in noncohesive bank materials, which is rooted in the widespread usage of the linear excess shear stress formulation (Eq. 1) that strictly applies only to cohesive sediment. The second question arises due to various terms being needed in Eq. (32) that cannot be established without the channel shape (e.g., $\eta|_{r_{thal}}$ and c_0).

A cross-sectional numerical framework very similar to that developed by Stecca et al. (2017) is implemented herein. A 1-dimensional (1D, r-direction) fixed (Eulerian) grid is used, which is discretized into numerical elements at equal spacing Δr. The center of each numerical element is referred to as the node; calculated variables are nodal values. The constant-width region of

numerical elements comprising the active channel is numbered as nodes 1 through N. The active channel intermittently shifts outward in discrete single-node increments based on physical processes, which are discussed in Section 4.4. When the active channel region shifts, the nodes are renumbered 1 through N in the new active channel region, and radial coordinates are reassigned to the fixed numerical elements to maintain r_{in}, r_{out}, and r_c constant within the active channel region. An illustration of the 1D domain is provided in Figure 7.

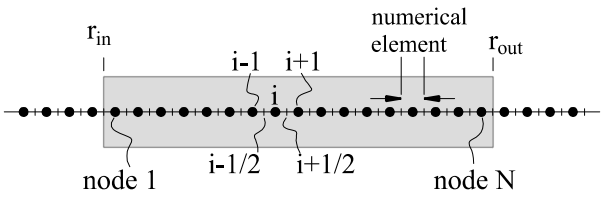

Figure 7: Plan view showing 1D configuration of nodes (i, i-1, i+1) and boundaries of numerical elements (i±1/2); the gray shading represents the active channel region of nodes that will shift rightward in time. A suitable spatial resolution is much denser than that shown; Δr is appropriately set to <0.1 x mean flow depth.

Quasi-steady, uniform, fully-developed bend flow is assumed, such that all divergence terms associated with mass and momentum fluxes in the *s*-direction are neglected. The parallel retreat cross-section under a specified bankfull discharge (Q_{bf}) is sought. Two required parameters are unknown: B and $\eta|_{r_{out}}$. The latter cannot be set arbitrarily high on the bank, as it potentially yields a condition in which more volume is eroded outside of the thalweg than can be deposited inside of the thalweg, thus preventing the development of steady-state migration. This issue is addressed in Appendix A, along with the rationale for establishing $\eta|_{r_{out}}$ as a function of B in Eq. (A12); therefore, only one unknown parameter B remains. The procedure is iterative, with an initial estimate of B and an arbitrary initial cross-sectional geometry specified. The numerical model contains two steps at each time interval, based on the quasi-steady approximation: (a) hydrodynamic calculation to obtain boundary shear stress distribution and subsequent calculation of q_{rt}; and (b) boundary deformation based on an explicit finite difference representation of Eq. (7). For the hydrodynamic calculation, rather than solving the mass and momentum conservation equations for the given Q_{bf} by solving the water surface elevation, $\xi(r)$, at each time step, an alternative procedure is used to reduce computation time. The transversely sloped water surface is maintained at the same elevations for nodes 1 through N throughout all time steps. The boundary shear stress distribution is calculated at each time step based on the momentum conservation equations. Q varies in time during the period of cross-section shape adjustment, since $\xi(r)$ is time-invariant, whereas $\eta(r)$

varies in time. The hydrodynamic calculations are detailed in Section 4.2; the bedload transport and boundary deformation calculations are detailed in Section 4.3.

The discrete time intervals between occurrences of active channel shifts defines ensembles of changing channel geometry between shifts in the Eulerian framework; steady state is considered to have been reached when cross-sectional geometries at specified times within ensembles have elevation differences within a specified tolerance. The ensemble comparison technique is described in Section 4.5. Once steady state is achieved, the calculated value of Q is evaluated with respect to the solution condition $Q = Q_{bf}$. If the condition is satisfied, the solution is complete; if it is not satisfied, then B is modified, and the procedure is repeated. The final solution is insensitive to the initial cross-section, provided that some portion of the initial cross-section is deep enough to yield $\tau_b > \tau_c$ at the bankfull flow level. All the parameters required for the model are provided in a table in the model application of Section 5.

4.2 Hydrodynamic Treatment

The key requirement of the hydrodynamic model is to reasonably represent the boundary shear stress distribution. The essence of the present treatment is the following assumptions: (a) the *s*-momentum equation is dominated by the driving force due to gravity and the resisting force due to fluid shear stresses; and (b) the *r*-momentum equation solution can be represented in an approximate manner using simplified formulations for transverse water surface slope and the deviation angle (δ) of the bed shear stress vector with respect to the *s*-direction. The momentum equations, including those terms that are neglected in this treatment, are detailed in Appendix B.

The *s*-momentum treatment is described first. Neglecting terms such as the radial and vertical transport of downstream momentum represents a somewhat crude approximation of the *s*-momentum equation when treating the near-bank region in bend flow. However, the simplified treatment that includes only gravity and boundary shear stress has proven to yield reasonably accurate results in meandering river morphodynamics simulations focused on bank erosion (Motta et al., 2014; Langendoen et al., 2016). The fluid shear stress on transverse faces of a control volume is considered a potentially dominant term in the *s*-momentum equation, particularly in the near-bank region. Therefore, control volumes are configured such that no *s*-directed shear stresses exist on the transverse faces (e.g., Pizzuto, 1990), as opposed to

establishing control volumes configured vertically. The nonvertical control volumes used in the hydrodynamic treatment warrants the clarification that the nodal positions in the 1D domain (Fig. 7) represent positions on the bottom boundary.

The specific method implemented to configure the control volumes with no fluid shear stresses on the transverse faces is the merged perpendicular method of Khodashenas and Paquier (1999), which is capable of treating concave-upwards, convex-upwards, and sharp-angled boundaries in the *r*-*z* plane. In this method, rays are extended upward-normal from the channel boundary until intersecting with the water surface or an adjacent ray. When two adjacent rays intersect, they are merged into a single ray segment beyond the intersection point; the merged segment is deflected intermediate to the orientations of the original rays. This yields a subdivision of the cross-section into adjacent nonoverlapping polygonal control volumes bounded by the rays. The rays originate from the bottom boundary at the lateral edges of each numerical element ($i \pm ½$; see Fig. 7). An illustration of the irregular control volumes based on this method are provided in Figure 8.

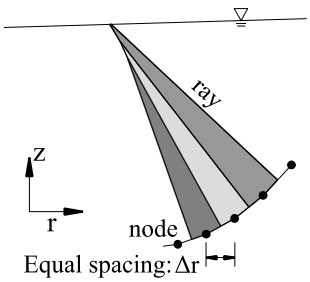

Figure 8: A conceptual illustration of three polygonal control volumes used to determine the boundary shear stress distribution in a small portion of the cross section. Note that polygons further to the left and right would alter the geometries of the three shown.

Rays are projected perpendicular to the boundary angle ω; for the ray projection, $\omega_{i+1/2}$ is calculated as $\tan^{-1}((\eta_{i+3} - \eta_{i-2})/(r_{i+3} - r_{i-2}))$, where the subscripts indicate the nodal position. Calculating $\omega_{i+1/2}$ in this manner effectively smooths the surface and is required to prevent numerical instability. The appropriate number of nodes to include in the smoothing decreases as the user-specified Δr value increases. Near nodes 1 and N, the number of nodes incorporated in the $\omega_{i\pm1/2}$ calculation is decreased to keep the smoothing window from extending beyond the limits of the active channel. Once the polygonal control volumes are geometrically defined, the local $\tau_{b,s}$ is calculated based on the force balance applied to the control volume. The downstream component of the water surface elevation gradient in fully developed bend flow is:

$$S \equiv \frac{d\xi}{ds} = \frac{S_c r_c}{r} \tag{34}$$

where S_c is the longitudinal slope along the channel centerline. The s-dimension at the bottom boundary equals $r\Delta\theta$. The uniform Δr spacing yields wetted perimeters of the numerical control volumes equal to $\Delta r/\cos\omega$. For all the calculations following the ray projection, $\tan\omega_i$ is calculated using central differencing between nodes i+1 and i-1, except at nodes 1 and N, which are one-sided calculations. Balancing the gravitational driving force with the boundary shear force acting on a polygonal control volume yields the following:

$$\tau_{b,s} = \rho g h' \frac{S_c r_c}{r} \tag{35}$$

$$h' = \frac{A_i}{(\Delta r/\cos\omega)} \tag{36}$$

where A_i represents the cross-sectional area of the polygon in the r-z plane. An assumption of Eq. (35) is that the s-dimension and radial coordinate of the control volume are approximately constant over the entire height of the polygon, which is reasonable, provided that the ray length is small relative to r. Following calculation of $\tau_{b,s}$ for each numerical node, a boxcar smoothing procedure is implemented that averages the boundary shear stress at the numerical node with the three numerical nodes on each side of it. The smoothing procedure has the same effect as the approach recommended by Khodashenas and Paquier (1999) that involves reducing the number of numerical elements for the boundary shear stress calculation; however, the smoothing eliminates the need to subsequently reassign intermediate $\tau_{b,s}$ values to the more densely spaced numerical elements through a curve-fitting procedure. Otherwise, the numerical routine is exactly as outlined in Khodashenas and Paquier (1999). Following calculation of $\tau_{b,s}$, the polygon-averaged velocity (U_i) is calculated using a standard bed shear stress closure, followed by the total discharge:

$$U_i = \left(\frac{\tau_{b,s}}{\rho C_f}\right)^{0.5} \tag{37}$$

$$Q = \sum_{i=1}^{N} U_i A_i \tag{38}$$

where C_f is the dimensionless friction coefficient, which is treated as a constant parameter in this analysis.

With respect to the *r* component of momentum, the goal is to establish reasonable approximations of the transverse water surface slope and $\tau_{b,rt}$. The Jansen et al. (1979) analysis based on Rozovskii (1961) is used for the transverse water surface slope:

$$\frac{d\xi}{dr} = \alpha_1 \frac{U^2}{rg} \tag{39}$$

$$\alpha_1 = \left[1 + 3\left(\frac{\sqrt{C_f}}{\kappa}\right)^2 - 2\left(\frac{\sqrt{C_f}}{\kappa}\right)^3\right] \tag{40}$$

where α_1 is a dimensionless coefficient whose value is very close to 1.0; and κ (=0.41) is von Karman's constant. Although dξ/dr is not strictly constant across the section, a representative value is sought for simplicity. A characteristic value of U is the depth-averaged velocity of a reference straight reach of the channel (U_0), characterized by a mean depth (H_0), and a roughness coefficient ($C_{f0} = C_f$). The depth-averaged s-momentum equation for the reference straight reach, assumed to have much greater width than the depth, allows U_0 to be calculated as:

$$U_0 = \left(\frac{gH_0S_c}{C_f}\right)^{0.5} \tag{41}$$

Note that the product U_0, H_0, and B_0 (the straight-channel reference width) is Q_{bf}, which provides a check on the reasonableness of the S_c and C_f parameters selected. Using U_0 and r_c as representative values in Eq. (39) yields:

$$\frac{d\xi}{dr} = \alpha_1 \frac{H_0S_c}{r_cC_f} \tag{42}$$

The current approach holds $\xi|_{r_{out}}$ constant at the outer bank floodplain elevation (η_{fp}) throughout the simulation; the remainder of the water surface is calculated according to:

$$\xi(r) = \xi|_{r_{out}} + (r - r_{out})\frac{d\xi}{dr} \tag{43}$$

At each time step, following calculation of the $\tau_{b,s}$ distribution, $\tau_{b,rt}$ is calculated using Eq. (28) and $|\boldsymbol{\tau_b}|$ is calculated according to Eqs. (29) and (30).

4.3 Bedload Transport and Boundary Deformation

The magnitude of the bedload transport rate vector $\boldsymbol{q}$ at each node is calculated using Eqs. (14), (15), and (17). The direction of $\boldsymbol{q}$ is calculated using Eqs. (19) and (24); since Eq. (19) is an implicit equation when using the nonlinear form of A in Eq. (24), a bisection scheme is used to solve tanβ numerically. The q_{rt} component of $\boldsymbol{q}$ is calculated according to Eq. (20). Following calculation of q_{rt} at all nodes, a temporally and spatially discretized form of Eq. (7) is used to calculate the bed elevation change at each time step:

$$\eta_i^{t+\Delta t} = \eta_i^t - \frac{1}{(1-\lambda)}\left[\frac{\Delta q_{rt}}{\Delta r} + \frac{{q_{rt}}_i^t}{r_i}\right]\Delta t \tag{44}$$

$$\frac{\Delta q_{rt}}{\Delta r} = \begin{cases} \frac{{q_{rt}}_{i+1}^t + {q_{rt}}_i^t}{2\Delta r} & \text{for i} = 1 \\ \frac{{q_{rt}}_{i+1}^t - {q_{rt}}_{i-1}^t}{2\Delta r} & \text{for i} = 2 \text{ to N} - 1 \\ \frac{-({q_{rt}}_i^t + {q_{rt}}_{i-1}^t)}{2\Delta r} & \text{for i} = \text{N} \end{cases} \tag{45}$$

where the subscripts after variable names indicate the spatial position and the superscripts indicate the time step. The formulations for $\Delta q_{rt}/\Delta r$ at nodes 1 and N are based on the boundary conditions that ${q_{rt}}_{1-1/2}^t = 0$ and ${q_{rt}}_{N+1/2}^t = 0$, while the interior node formulation is based on central differencing.

4.4 Grid Translation

Translation of the active channel region occurs due to bedload transport processes at node N. The $q_{rt}|_{r_{out}} = 0$ boundary condition ensures that node N is degradational, provided that $\boldsymbol{\tau_b} > \tau_c$ at node N; (this latter condition is described later in this section.) The slope angle that develops between node N-1 and node N is projected to the top of the noncohesive layer following boundary deformation as shown in Figure 9; the variables $\Delta z_{N,N-1}$ and $\Delta z_{N+1,N}$ are defined on the figure. When $\Delta z_{N,N-1} \leq \Delta z_{N+1,N}$, then the projected slope intersects the top of the noncohesive layer at, or to the right of, node N+1. When that occurs, then node N+1 becomes incorporated into the active channel at the next time step. All nodes i = 1 to N+1 are then renumbered according to: $i_{t+\Delta t} = i_t$ - 1. Conceptually, this assumes the upper noncohesive layer fails vertically at node N+1. The r coordinates of nodes 1 through N maintain the same values before and after the grid translation.

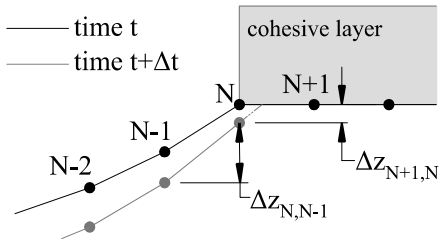

Figure 9: Bank profile that illustrates the evaluation procedure for specifying outward translation

Another potential cause of grid translation is mass failure within the noncohesive layer. Oversteepening of the noncohesive soil to angles greater than the friction angle (Φ) will lead to shallow planar failures (Thorne, 1982). Although Φ (a mass property of the soil), and θ_{rp} (a property of grains) can potentially have different values, the two are conventionally assumed to be equivalent. This is valid in the case of an unstructured noncohesive deposit, as assumed in the present analysis; for the alternative case, see Millar and Quick, (1993) and Darby et al. (2007). Oversteepening will occur when an interface develops on the slope in which $\boldsymbol{\tau_b} = \tau_c$, causing the lower slope ($\boldsymbol{\tau_b} > \tau_c$) to deform, while the upper slope ($\boldsymbol{\tau_b} < \tau_c$) remains static. This steepens the slope near the interface and creates a topographic discontinuity (Kovacs & Parker, 1994). However, the present model simulates bankfull flow, in which the noncohesive layer is always submerged. Even where the boundary shear stress becomes very small, the transverse slope steepens to the condition in which bedload transport occurs over the entire bank profile, because as ω approaches θ_{rp}, τ_c approaches zero. Extensive simulations revealed that slopes greater than θ_{rp} do not develop during the evolution toward the parallel retreat profile when using the assumption that $\Phi = \theta_{rp}$; only a specified over-steep initial condition yields a situation in which a mass failure algorithm is warranted for the noncohesive bank material. Therefore, a planar failure algorithm is not relevant to the present analysis, although details of the one developed when considering sub-bankfull flow can be found in Waterman (2017).

4.5 Ensemble Comparison for Steady State Determination

In the Eulerian model framework, η changes at every node at every time step; steady state must be evaluated in this context. The number of time steps between consecutive channel shifts defines an ensemble of n_{ens} cross-sections. Once the parallel retreat condition is achieved, n_{ens} reaches a constant value or oscillates around a constant value when the time between shifts is not

an integer multiple of Δt. Comparisons of the η values are made with respect to two ensembles that are separated by a lateral migration distance equal to H_0. These are referred to as Ensemble 1 and Ensemble 2. The cross-sections at five discrete time positions within Ensemble 1 and Ensemble 2 are compared: $0.2n_{ens}$, $0.4n_{ens}$, $0.6n_{ens}$, $0.8n_{ens}$, and $1.0n_{ens}$. At each of these five times, the η values for that cross-section within Ensemble 1 and Ensemble 2 are compared at all spatial nodes 1 through N, and two error values, E_1 and E_2 are calculated as:

$$E_1 = \frac{1}{5N}\sqrt{\sum_{j=1}^{5}\sum_{i=1}^{N}\left(\eta_{i,Ens1} - \eta_{i,Ens2}\right)^2} \tag{47}$$

$$E_2 = \max_{j=1\rightarrow 5, i=1\rightarrow N}\left|\eta_{i,Ens1} - \eta_{i,Ens2}\right| \tag{48}$$

where the subscripts indicate the following: i, the spatial node; j, the cross-section evaluated within the ensemble; *Ens1*, Ensemble 1; and *Ens2*, Ensemble 2. The error term E_1 is the root mean square deviation over all nodes and cross-sections evaluated, and E_2 is the maximum individual deviation at a node. The steady-state criteria used requires both of the following conditions be satisfied: (a) $E_1 \leq 1\text{x}10^{-5}H_0$; and (b) $E_2 \leq 1\text{x}10^{-4}H_0$. Following achievement of steady-state migration, the calculated Q from Eq. (38) is evaluated according to the criteria: $|Q - Q_{bf}| \leq 0.001Q_{bf}$. If the criterion is not satisfied, then the procedure begins again with an increased B value when $Q < Q_{bf}$ or a decreased B value when $Q > Q_{bf}$.

5 Application of Numerical Model: Lower Mackinaw River

5.1 Study Site Description

The Mackinaw River is a gravel-bed, single-thread, meandering river that is a large tributary of the Illinois River in the state of Illinois, central United States. The basin area is 2976 km^2 (Fig. 10a and 10b). The river is approximately 203 km long, with a mean longitudinal slope of 0.00056 and minimal slope variation along its length. The field study site and the nearest flow gauge station are located 12.7 km and 27.3 km upstream of the Illinois River confluence, respectively. The USGS (U.S. Geological Survey) gauge station, number 05568000, has been operated continuously from 1921 to 2020. The mean daily discharge is 21.9 m^3/s and the 2-year recurrence interval annual series peak flow is 237 m^3/s; an inflection in the gauge station rating curve is present at approximately Q = 241 m^3/s, which suggests overbank flow is initiated at the

741 gauge station at approximately the 2-year recurrence flow. The bankfull flow (Q_{bf}) is estimated
742 to be 240 m^3/s at the field site.

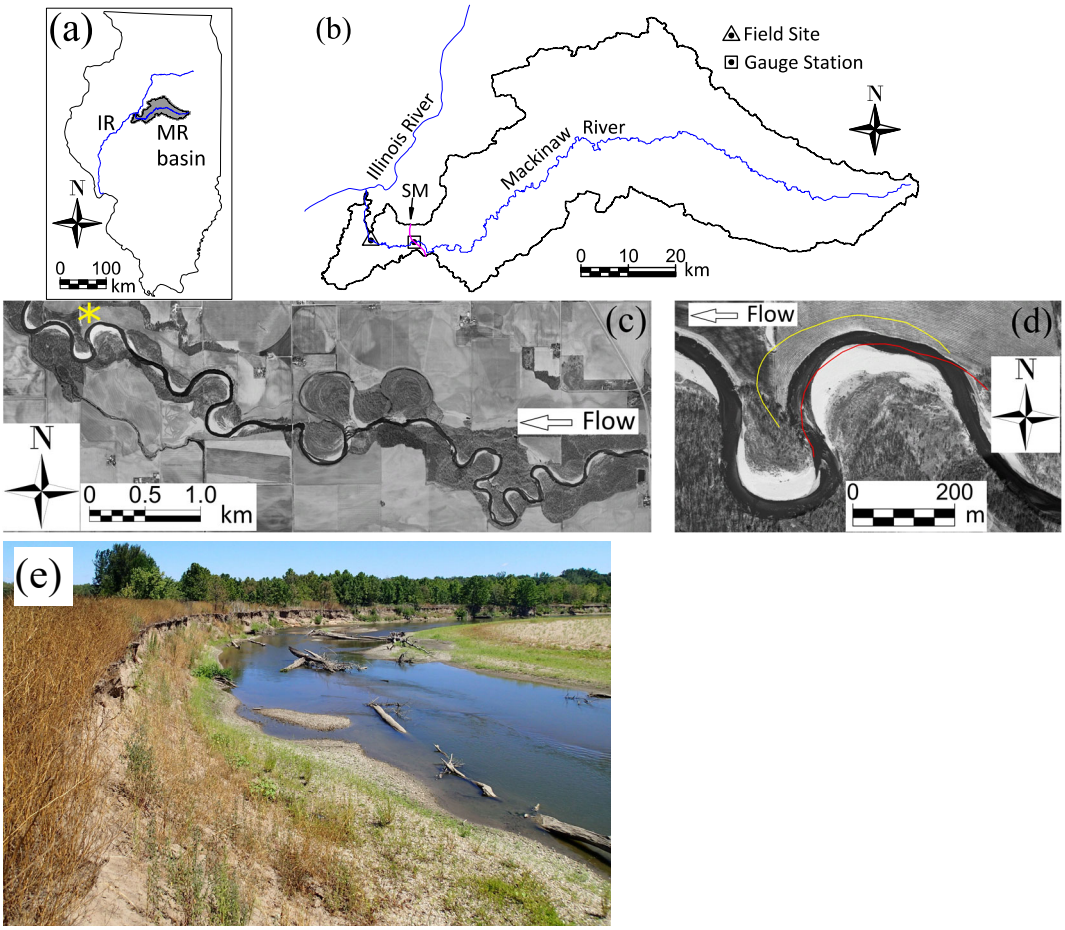

743 **Figure 10**: Illustration of the study site at increasing scales; (a) the Mackinaw River (MR) basin relative to the
744 Illinois state boundary and the Illinois River (IR); (b) basin scale view showing location of the west terminus of the
745 Shelbyville moraine (SM), the field site, and the stream gauge station; (c) Google Earth aerial photograph from
746 04/02/05 of lower Mackinaw River with the study bend demarcated with the asterisk; (d) the same 04/02/05 aerial
747 photograph zoomed into the study bend, where the red line is the digitized outer bank from 04/16/1998 and the
748 yellow line is the digitized outer bank from 06/16/2016; (e) site photograph from 2012 looking upstream along the
749 outer bank from the downstream end of the study bend.

750 The basin topography is dominated by a sequence of roughly parallel morainal ridges aligned in
751 a general northwest to southeast direction, with the westernmost being the Shelbyville moraine
752 (Fig. 10b). The Mackinaw basin west of the Shelbyville moraine is a broad valley containing
753 predominantly sand and gravel glacial-fluvial deposits, formed by glacial outwash torrents
754 (Johnston, 2003); these deposits have been reworked by the modern river and include post-
755 glacial alluvium. The submorainal Mackinaw River located west of the Shelbyville moraine
756 terminus is a geomorphically distinct unit of the river (Gough, 1994) subject to high migration

rates, frequent cutoffs, and a relatively large width-depth ratio, due largely to the predominantly noncohesive lower bank materials. The field site is an actively migrating bend that contains composite banks with a 4 m typical height from thalweg to top of bank. The upper cohesive layer comprises approximately half of the bank height and stands nearly vertical; the lower noncohesive layer of sand and gravel comprises the remaining half of the height and is generally convex-upward in cross-section with a much milder transverse slope. As shown in Figure 10d, the study bend has migrated extensively between 1998 and 2016; the maximum bank migration at the bend apex is 102 m, or approximately 5.6 m/yr. The lower bank commonly contains slump blocks from the upper layer that develop annual vegetation if allowed to persist for sufficient duration without being eroded (Fig 10e).

5.2 Field study

The analytical and numerical treatments represent a canonical case based on assumptions that will never be realized under real conditions. Thus, the field study was performed only to ascertain whether the canonical case reasonably approximates field conditions with respect to cross-sectional shapes and migration rates predicted. Two topographic surveys were performed using conventional total station survey methods and a local horizontal/vertical datum. The first survey was performed on September 19-20, 2013 during low flow (1.41 to 1.78 m^3/s). The second topographic survey was performed on September 29-30, 2015 during moderately low flow (8.16 to 9.10 m^3/s). Both surveys were performed after spring flood events with $Q > Q_{bf}$ with no geomorphologically active events between the flood events and the respective surveys, with the intent for the surveys to represent reshaped channel geometry due to recent large flood events. The flow record at the gage station is illustrated in Figure 11.

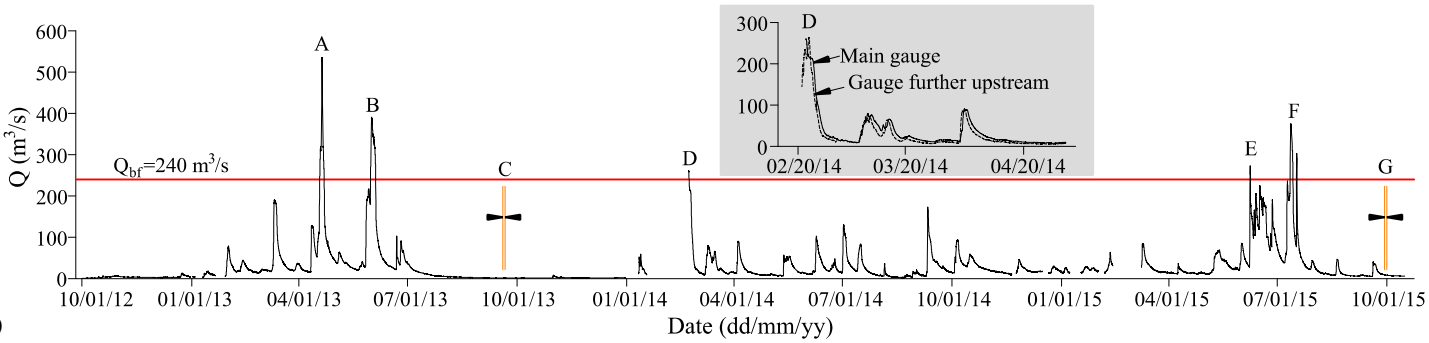

Figure 11: Discharge record from USGS station 05568000 just upstream of the site. The field surveys were performed during the periods labeled 'C' and 'G'. Flood events are labeled 'A', 'B', 'D', 'E', and 'F'. Periods with

782 no data are due to ice. The gray inset that contains the event labeled 'D' includes the record from station 05568000
783 and the next gauge station upstream, 05567500; the latter captured more of the short winter event and is considered
784 to be the best available approximation of discharge conditions at station 05568000.

785 The topography was not obtained along monumented cross-sections; rather, data points were
786 collected to represent full coverage of the banks, channel, and point bar. The 2015 topographic
787 survey focused on the downstream portion of the bend subjected to the highest migration rates. A
788 triangular-irregular-network (TIN) was created for each survey, and the topography for the cross-
789 sections were sampled from the TINs. The cross-sectional locations are shown in Figure 12.
790 Each cross-section had similar characteristics when comparing the 2013 and 2015 data, with the
791 sections translated outward with discernible but minor changes in shape. In Figure 13, Cross
792 Section D illustrates representative conditions; at this section, the data transects on the banks
793 from 2013 and 2015 were directly in alignment, and thus, interpolation errors associated with
794 sampling from the TIN in the bank region are minimized. Between cross sections C and F, the
795 channel migrated an average of 8.15 m with a maximum of 10.8 m; the average was obtained by
796 calculating the area between the top of bank lines shown on Figure 12 and dividing by the
797 average length of the top of bank lines between those sections. In addition to the topographic
798 data, surface soil samples of the bank were collected and surveyed in 2013 between Cross
799 Sections C and D. The locations of these samples are shown on Figure 13. From the water line to
800 the top of the noncohesive layer, the soil became finer-grained upwards in a similar manner to
801 that observed on the point bar. The grain-size distributions are illustrated in Figure 14.

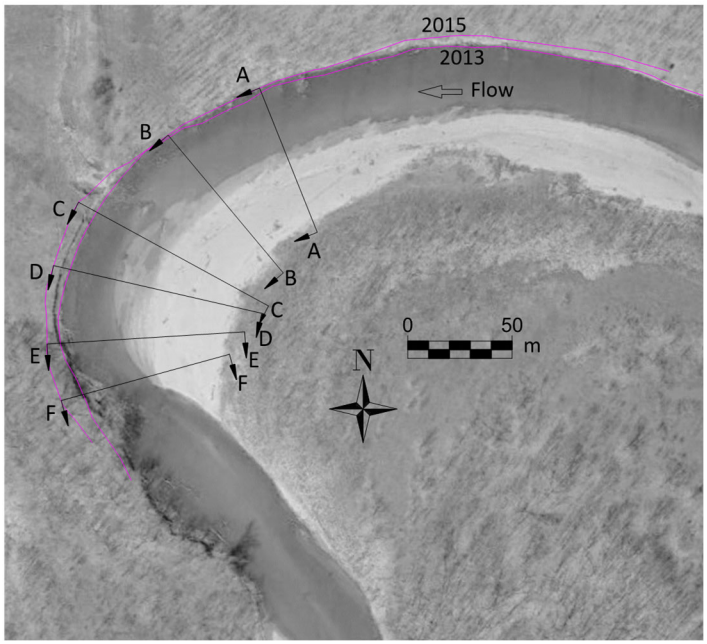

Figure 12: Cross sections from topographic survey overlain on the Google Earth aerial photograph from 04/17/2014. The two magenta lines are the surveyed top of bank from the field surveys in 2013 and 2015.

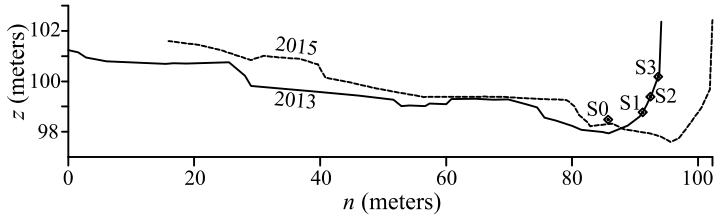

Figure 13: Cross-section D as surveyed in 2013 and 2015. The transverse coordinate n is used, where $n = 0$ is relative to the end of the cross-section illustrated in Figure 12. The vertical is exaggerated 4x. The marks S0 through S3 are the locations of the surface soil samples. Sample S0 was from a low midchannel bar located off the cross-section; S1, S2, and S3 were sampled on the bank.

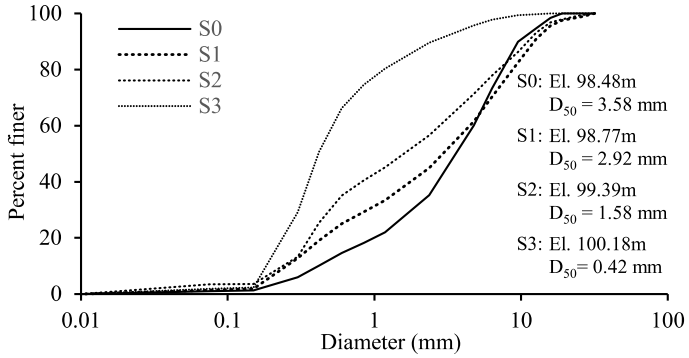

Figure 14: The grain-size distributions of the bank and bar samples.

5.3 Numerical model results and comparison with field data

The results of three different simulations are illustrated; all parameters used in the simulations are identical, except the D_{50} and τ^*_{c0} values. Simulation 1 has D_{50} = 3.5 mm and τ^*_{c0} = 0.036. Simulation 2 has D_{50} = 7.5 mm and τ^*_{c0} = 0.040. Simulation 3 has D_{50} = 15.0 mm and τ^*_{c0} = 0.045. As few grains were recorded in the sediment samples with D > 15 mm (maximum 4% mass for grains coarser than 15 mm in sample S1), simulations were not extended to greater D_{50} values. The full list of parameters is provided in Table 1. The values for B_0 and r_c were estimated based on aerial photograph analysis; H_0 was an estimate based on field observations; S_c was based on longitudinal profiles of the river (Gough, 1994); and Q_{bf} was based on data analysis from the nearby gage station. Figure 15 and Table 2 illustrate the results of the simulations.

Table 1: List of parameters used in the numerical simulations. The equation column indicates how the parameter is used in the numerical model; the parameter may be in other equations that are part of the analytical treatment that are not provided in the table.

Parameter	Value	Eqn.
B_0 (m)	50.0	41
C_f	0.0059	37, 40
D_{50} (mm)	3.5	18, 20
H_0 (m)	3.0	41
K_0	5.7	17
K_1	10	28
Q_{bf} (m^3/s)	240	38
r_c (m)	150	34, 35
R_s	1.65	18, 20
S_c	0.00056	34, 35
Δr (m)	0.1	36, 45
Δt (s)	30	44
θ_{rp} (°)	40	15, 16, 24
λ	0.40	44
μ_d	0.5	24
τ^*_{c0}	0.036	14, 17, 18, 19
χ	1.0	24

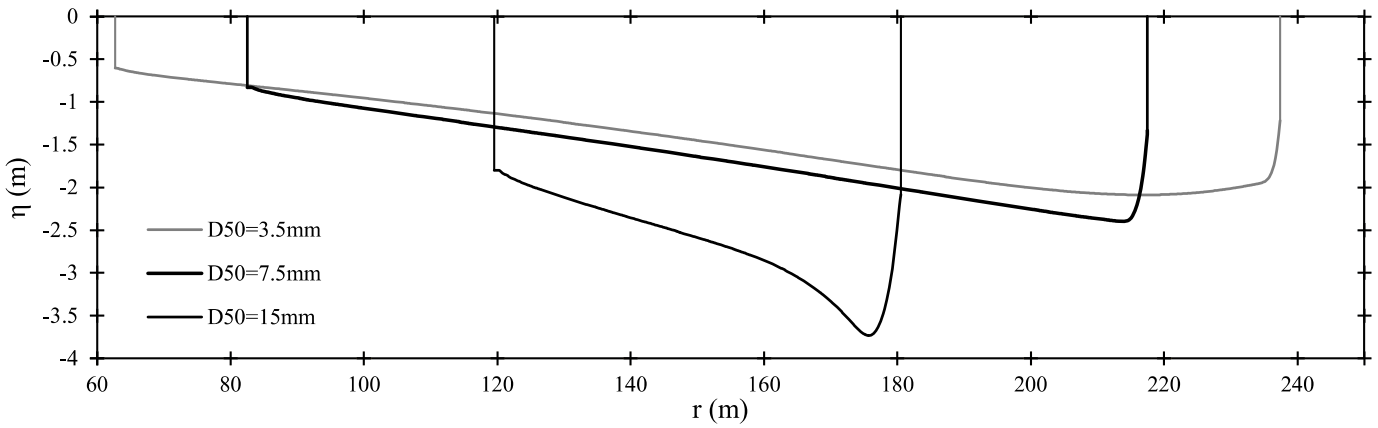

Figure 15: The steady-state migrating cross-sections for the three simulation conditions. Vertical lines are used to illustrate the lateral boundaries (cohesive top layer on right bank; vegetated over-bar region on left bank).

Table 2: Results of numerical simulations.

	Sim. 1 D_{50}=3.5 mm τ^*_{c0}=0.036	Sim. 2 D_{50}=7.5 mm τ^*_{c0}=0.040	Sim. 3 D_{50}=15.0 mm τ^*_{c0}=0.045
B (m)	174.7	135.0	61.0
r_{thal} (m)	216.80	213.85	175.65
$\eta\|_{rout}$ (m)	-1.221	-1.335	-2.085
$\eta\|_{rthal}$ (m)	-2.088	-2.400	-3.735
$h\|_{rthal}$ (m)	2.05	2.39	3.73
$\tau^*_s\|_{rthal}$	0.137	0.0735	0.0611
c_0	0.999	0.969	0.848
$q_{rt}\|_{rthal}$ (m^2/s)	-1.45x10^{-5}	-1.05x10^{-5}	-1.96x10^{-5}
$\int_{r_{thal}}^{r_{out}} \frac{q_{rt}}{r} dr$ (m^2/s)	-1.14x10^{-6}	-1.32x10^{-7}	-3.74x10^{-7}
M (m/day)	2.21	1.40	1.67

The η values are relative to a vertical datum at the floodplain surface elevation (top of cohesive layer); c_0 is back-calculated from Eq. 26(a) using the outputs of the hydrodynamic variables. The M values are the migration rates recorded in the simulations; when using the model outputs of sediment transport rates and geometry variables, all migration rates were confirmed to be equivalent to the calculated value using Eq. (25). Simulation 1 has the sediment parameters that best represent the field data, but the result does not accurately represent the cross-sectional shape observed in the field; increasing D_{50} and τ^*_{c0} for Simulations 2 and 3, the results approach the observed cross-sectional shapes. The simulation results suggest the Mackinaw River behaves according to a considerably higher τ_{c0} than that indicated by the grain size distribution observed

in the field, which is a key issue discussed in the Discussion and Conclusions. The numerically generated cross-section and field surveyed sections are compared in Figure 16.

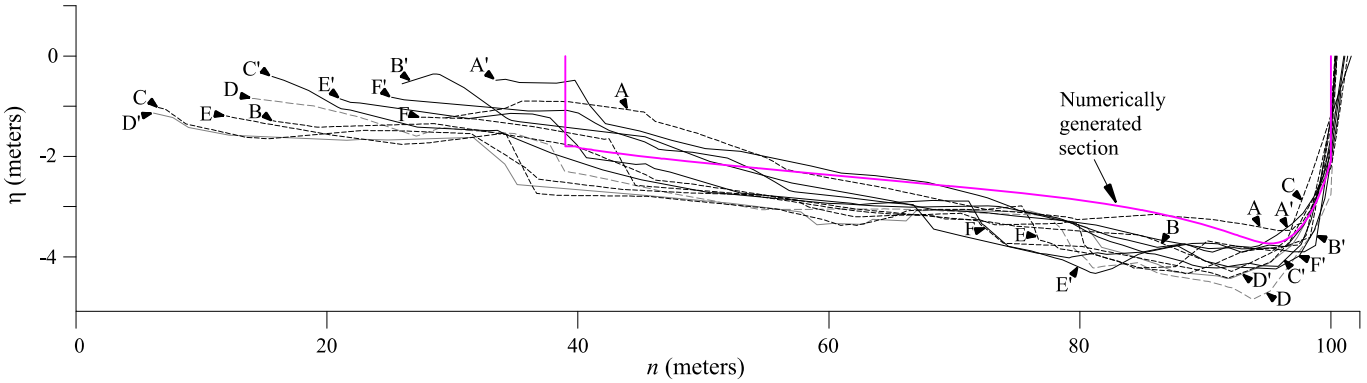

Figure 16: The black cross-sections are Cross Sections A through F surveyed in 2013 (dashed lines) and 2015 (solid lines, section name appended with '). Positions of cross-sections are shown on Fig. 12. All cross-sections are placed on same frame of reference for comparison by setting top of bank elevation to η = 0.0 m; and the n position of the top of noncohesive layer to 100.0 m. The magenta line is the numerically generated cross-section using D_{50}=15 mm and τ^*_{c0}=0.045.

Figure 17 illustrates a time series of the cross-section evolution from an arbitrary initial condition to the steady-state configuration for the simulation with D_{50} = 15mm. As the water surface elevation is kept steady in time, the discharge changes until the steady-state configuration is achieved. Figure 18 illustrates the distribution of τ^*_s and q_{rt} associated with the steady-state configuration.

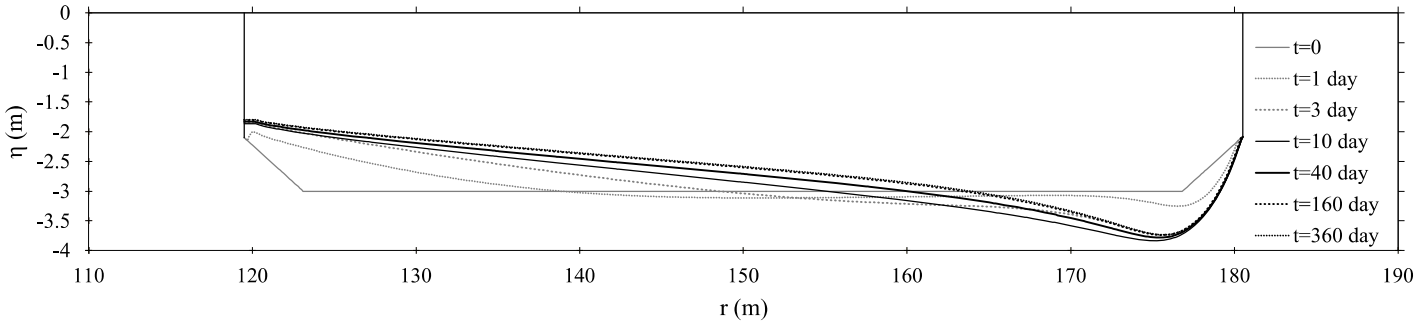

Figure 17: Time evolution of the simulation performed with D_{50} = 15 mm and τ^*_{c0} = 0.045.

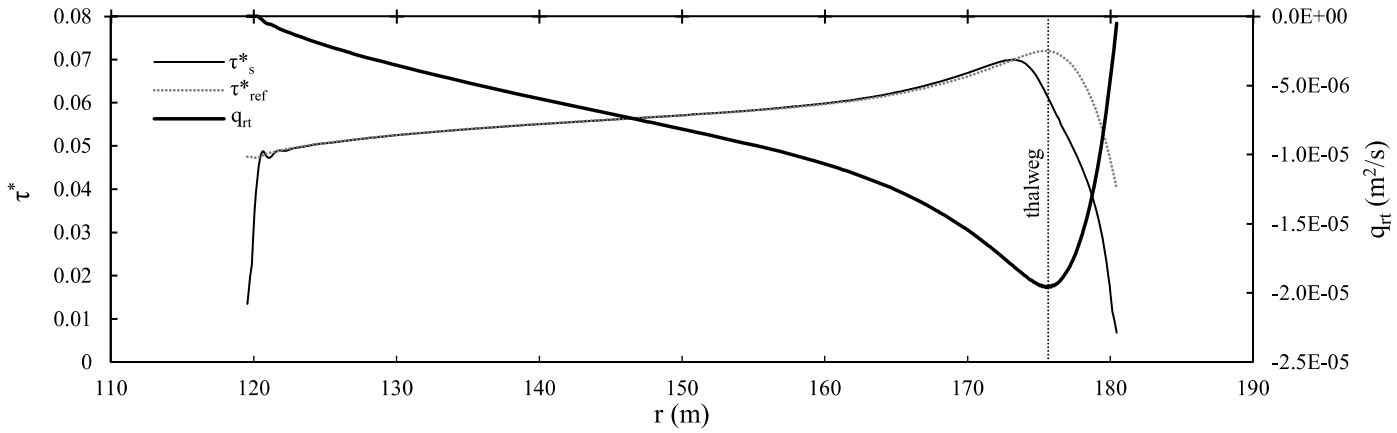

Figure 18: Steady-state distribution of τ^*_s and q_{rt} for the simulation performed with D_{50} = 15 mm and τ^*_{c0} = 0.045. Note that τ^*_{ref} is a calculated reference value based on $\tau_b = \rho g h S$, which neglects momentum extraction due to shear on transverse faces.

The numerical model simulates migration under a steady Q_{bf}. The meander bend at the field site underwent migration and cross-sectional reshaping over a range of flows that included Q_{bf}; therefore, comparison of the migration rates between the field site and the simulations are approximate and indicate only whether the migration rates are on the right order of magnitude. Between the 2013 and 2015 surveys, the surveyed region in Fig. 12 experienced an average migration distance of 8.15 m (maximum 10.8 m). Using the 15-minute time series at the USGS gage station, $Q \geq Q_{bf}$ was experienced for 3.26 days between the surveys; and $Q \geq 0.8Q_{bf}$ was experienced for 10.54 days. Assuming migration only occurred when $Q \geq Q_{bf}$ suggests a mean migration rate of 2.5 m/day and assuming migration occurred throughout the period $Q \geq 0.8Q_{bf}$ suggests a mean migration rate of 0.77 m/day. The simulation result of 1.67 m/day migration rate lies between these two values, and thus, it suggests the simulated migration rate is within the proper order of magnitude. As another check on the reasonableness of the results, the aerial photograph illustrated in Fig. 10d shows digitized bank lines over the 18.2-year period of migration between 1998 and 2016. The maximum migration rate was 102 m. Using the 15-minute time series, $Q \geq Q_{bf}$ was experienced for 47.8 days during this time period; and $Q \geq 0.8Q_{bf}$ was experienced for 81.9 days. Assuming migration only occurred when $Q \geq Q_{bf}$ suggests a mean migration rate at the locus of maximum migration equal to 2.1 m/day and assuming migration occurred throughout the period $Q \geq 0.8Q_{bf}$ suggests a mean migration rate of 1.1 m/day. As before, the results suggest the order of magnitude predicted by the simulations is correct.

6 Discussion and Conclusions

6.1 General Considerations

The analysis presented is a conceptualization intended to shed light on bank erosion and channel migration when noncohesive bank material is a dominant factor. Such a treatment highlights key physical processes and provides a basis for comparison with observations to provide clues to those factors responsible for deviations from the canonical case. The three objectives outlined in the Introduction were resolved: (a) a rational constraint on the bank shape was established ($\omega|_{r_{thal}}=0$); (b) a migration rate formulation was developed (Eq. 32); and (c) parallel retreat was shown numerically to develop as conceived in the analytical treatment as a simple outward translation of the cross-section rather than involving a cyclic process of basal erosion and mass failure in the noncohesive layer. The findings reveal important differences to past treatments; they also highlight important aspects of channel shape and misunderstandings that can result from usage of the linear excess shear stress formulation (Eq. 1) when modeling bank deformation in noncohesive materials.

The analytical treatment focused on the development of a steady-state migration rate equation based on integration of the Exner equation over the bank region following the logic of Hasegawa (1989), which requires calculation of $q_{rt}|_{r_{thal}}$. Since $q_{rt}|_{r_{thal}}$ is dependent on the local transverse slope at the limit of integration, the slope should not be assigned arbitrarily. The $\omega|_{r_{thal}}=0$ shape constraint determined theoretically and confirmed numerically yields a substantially different migration rate equation than that of Hasegawa (1989), due to a change in the dominant factors that dictate $q_{rt}|_{r_{thal}}$, which drives migration. Equation (19) indicates that the decomposition of $\boldsymbol{q}$ at any point has a contribution associated with secondary flow (the term containing tan δ) and a contribution associated with transverse slope (the term containing tan ω). Whereas Hasegawa (1989) determined that the contribution from secondary flow was small enough to be neglected, the current analysis finds that the contribution from the secondary flow is responsible for the entirety of the transverse component of the bedload transport rate at the thalweg when considering the case of parallel retreat. This yields a migration rate equation (Eq. 32) that is dependent on curvature, unlike previous forms of migration rate developed using the integral treatment. Previous bank-integrated migration rate formulations implicate the helical flow

908 associated with curvature indirectly, as it is responsible for a deeper channel near the outer bank,
909 which results in excess velocity or excess boundary shear stress near the outer bank. The present
910 model more directly implicates the importance of curvature in the migration process as the
911 primary driver of the transverse rate of bedload transport due to the helical flow. The migration
912 rate formulation developed also generalizes to the case of a straight channel, in which $r = \infty$ and
913 consequently $M = 0$.

914 The analysis supports a finding of Stecca et al. (2017), who evaluated a number of variables for
915 suitability as independent variables in lumped noncohesive bank migration formulations. Among
916 the variables analyzed, the downstream component of sediment transport rate at the basal node
917 was deemed among the most promising. The current analysis indicates the physical basis of this
918 finding, in that the migration rate is based on $q_{rt}|_{r_{thal}}$ which is directly related to $q_s|_{r_{thal}}$ through the
919 variable β (which is equal to δ at the thalweg). Another interesting finding is that the Selwyn
920 River cross-sections they analyzed for a hydrograph that produced bankfull flow resulted in
921 cross-sections that maintained their general shape after undergoing a migration distance of > 15
922 m, similar to that documented in the present study. The shapes were also qualitatively similar to
923 those of the present study, being concave-upward on the bank and across the thalweg and
924 transitioning to convex-upward on the bar.

925 A substantial body of research has addressed equilibrium channel cross-sectional geometry in
926 straight channels with noncohesive banks and equilibrium point bar geometry when the outer
927 bank is fixed (nonmigrating). A migrating channel differs from both scenarios. The past
928 treatments involved the channel achieving a shape such that $q_{rt} = 0$ everywhere on the section.
929 The current treatment does not invalidate those approaches; however, it does show that such a
930 solution is specific to the case in which $M = 0$. The more general solution is expressed in Eq.
931 (10), which is valid for either a migrating or non-migrating steady-state condition. For $M > 0$, q_{rt}
932 will be negative across the section except near the boundaries (where $q_{rt} = 0$ as specified
933 boundary conditions). This is illustrated in the numerical results of Fig. 18 but can also be
934 substantiated theoretically. At the thalweg, a negative q_{rt} is ensured due to the secondary flow
935 direction in conjunction with the $\omega|_{r_{thal}} = 0$ shape constraint. Assuming that the value q_{rt}/r is small,
936 Eq. (10) indicates the negative q_{rt} will be approximately the local minimum ($\partial q_{rt}/\partial r \approx 0$ where
937 $\partial\eta/\partial r = 0$). Moving in the positive r direction (bankward of the thalweg), where $\partial\eta/\partial r$ is positive,

Eq. (10) requires a less negative q_{rt} that will transition to $q_{rt} = 0$ at the boundary. Moving in the negative r direction, where $\partial\eta/\partial r$ is negative, Eq. (10) also requires a less negative q_{rt} that will transition to $q_{rt} = 0$ at the boundary. The analysis has not advanced to the point of being able to specify $\eta|_{r_{thal}}$ or r_{thal} without the use of the numerical model. However, if these variables could be predicted, it is conceivable that Eq. (10) could be used to calculate steady-state migrating shapes analytically in an analogous manner to past work using the $q_{rt} = 0$ solution criteria (e.g., Kikkawa et al., 1976). Such an analysis would be most practicable interior to the thalweg (well away from the outer bank), where the boundary shear stress is readily determined as a function of the local flow depth (see Fig. 18).

While the exact cross-section shape still cannot be specified without detailed numerical analysis of the hydrodynamics and the transverse boundary layer associated with the outer bank, both the analytical and numerical treatments indicate that the shape will have differences relative to the characteristic cross-section of Parker et al. (2011) depicted in Fig. 6. The convex-upward shape of the region left of the thalweg in Fig. 6 is based on the $q_{rt} = 0$ solution criterion used for predicting the transverse slope on the point bar. The convex-upward shape on the bar is valid, although the results illustrated here suggest that the convexity is poorly pronounced during steady-state migration, having only a slight camber similar to the point bar platforms described by Nanson (1980), on top of which scrolls of finer-grained suspended material were deposited. Further comparison with the characteristic cross-section of Parker et al. (2011) reveals more significant differences at the thalweg and in the bank region. A concave-upwards shape develops interior to the thalweg, with a horizontal transverse slope at the thalweg, and with the concave-upward shape continuing throughout the noncohesive layer bankward of the thalweg. This is contrasted with the grade break at the thalweg in Parker et al. (2011) in which the convex-upward topography interior to the thalweg abruptly changes to a uniform slope in the bank region. The Mackinaw River field data provides one example that the cross-sectional shape suggested by the present analysis is more realistic for a migrating meander bend with composite banks.

The concave upward shape within the noncohesive material in the bank region directly contradicts the shape suggested by use of the linear excess shear stress equation (Eq. 1) to model noncohesive fluvial erosion. Applying Eq. (1) to bank materials consisting of uniform soil

properties suggests the following: (a) because the boundary shear stress generally increases with depth, the erosion rate will be greatest near the base of the bank, thus, leading to steepening in the presence of excess boundary shear stress; (b) continued steepening leads to an unstable bank slope that exceeds the soil friction angle and large-scale mass failure involving much of the bank height; (c) after failure, the basal material must be removed by fluvial action; and (d) the cycle repeats. Such cyclical behavior would violate the basic assumptions of the parallel retreat conceptualization of a bank migrating without changing shape. While the cyclical sequence described accurately characterizes the process for cohesive bank erosion, it inaccurately characterizes the process for noncohesive bank materials mobilized as bedload. When implementing the Exner equation with a suitable bedload transport relationship, a boundary shear stress distribution that increases with depth does not cause a bank slope to steepen with depth, but rather causes the slope to relax with depth. The development of a concave-upward noncohesive bank shape in the presence of excess boundary shear stress has been well documented experimentally in straight channels (e.g., Ikeda et al., 1981). As is borne out by the present analysis, the resulting shape does not fundamentally change simply due to the addition of planform curvature. The primary difference between the straight channel case and the bend flow case is that the helical flow serves to drive a transverse component of bedload away from the base of the outer bank. This allows the bank to migrate when subjected to excess shear stress rather than aggrading the base and relaxing its slope to a threshold channel configuration as occurs in the absence of the helical flow. One way to generalize between straight and curved channels is by conceiving of a "demand" for bed material imposed by the removal of sediment at the base of the bank in the transverse direction, following Thorne (1982) regarding unimpeded removal of basal material. When the channel is straight, the bed material demanded at the base of the bank is zero; when the channel has curvature, the demand is non-zero. This demand is satisfied through the adjustment of bank shape, which affects both the boundary shear stress distribution and the transverse component of bedload. Thus, analogous to the concept of a graded channel which delicately adjusts its longitudinal slope to convey exactly the sediment fed into the stream with the available discharge (e.g., Mackin, 1948), the steady-state migrating channel delicately adjusts its transverse slope to satisfy the demand for material at the base of the bank in a manner that conforms with Eq. (10).

The findings also shed light on laboratory experiments involving meandering channels in noncohesive materials. With reference to Fig. 3, two primary reasons can be identified for the difficulty in achieving a condition approximating parallel retreat in laboratory experiments of meander bend evolution: (a) vegetation establishment and consequent fine sediment deposition in over-bar Region 3 is not able to suitably constrain the channel geometry on the inner bend; and (b) $\eta|_{r_{out}}$ is commonly set too high on the outer bank relative to the elevation at which the sediment can be transported at the inside of the bend, which creates the condition in which the cross section will be net aggradational as it migrates, as demonstrated in Appendix A. This widening and shallowing of the channel during migration ultimately devolves into a braided channel form. Both conditions could potentially be mitigated through appropriate experimental setup and procedures undertaken during an experiment to artificially incorporate point bar vegetation. However, a third issue of bank stiffening to artificially slow the outer bank migration appears to be an additional step that is warranted to best represent prototype conditions based on the present findings. As evidence, the Mackinaw River appears to behave as if the critical shear stress is considerably larger than that indicated by its grain-size distribution. This is discussed further in the following subsection.

6.2 Limitations and Practical Considerations

The highly conceptualized scenario analyzed in this study is a gross simplification of the complexities of real rivers; it is intended as a canonical case. Nevertheless, some practical application of the analysis can be anticipated for use in lumped bank erosion models. The concepts developed would be most useful in a lumped bank erosion model if a similarity function for the bank shape had been obtained. The analysis did not progress to the stage of being able to specify such a function. Nevertheless, the demonstration of the concave-upward bank shape with the $\omega|_{r_{thal}}=0$ shape constraint that precludes a cyclical process of oversteepening and mass failure in coarse noncohesive bank materials has significant modeling implications. The $\omega|_{r_{thal}}=0$ shape constraint that is valid for steady-state migration seems to reasonably represent the field data, and this constraint allows ready calculation of the transverse component of the bedload transport rate that drives the bank migration rate in either Eq. (25) or Eq. (32). Figure 18 shows that the bank maintains its concave upward shape during shape evolution, and thus, the $\omega|_{r_{thal}}=0$ shape constraint appears reasonable even during unsteady-state migration. The

numerical model whose bank erosion treatment most closely approximates the present treatment is that of Nays2DH (Shimizu et al., 2014; Eq. 129 therein). In that model, a bank erosion formulation nearly equivalent to Eq. (25) is used, although it incorporates an additional term based on aggradation or degradation of the basal node. The basal node elevation change is from an independent Exner equation calculation that incorporates the spatial derivatives of the sediment transport vector $\boldsymbol{q}$ in both the r and s directions. That model or any other model that explicitly calculates $\boldsymbol{q}$ at the basal node can readily incorporate the $\omega|_{r_{thal}}=0$ shape constraint to better approximate a similarity function over the bank region rather than assuming the basal node represents an abrupt grade break associated with a bank of constant slope.

Any model that simulates hydrographs of individual events must recognize that a variable discharge will result in bank reshaping not accounted for in a lumped bank erosion model that assumes a similarity function for bank shape. A change in the bank shape will yield periods where the top of bank migrates greater and lesser distances than that suggested by the transverse flux of sediment at the base. However, over long periods of time, such as dealt with in models such as RVR Meander (Abad & García, 2006; Motta et al., 2012), these transient periods of bank reshaping will average out, and the volume of sediment transported transversely across the thalweg will approach the volume of noncohesive bank material contained in the calculated migration distance. Models such as RVR Meander that assume a cross-sectional form rather than calculating bed evolution explicitly using the Exner equation present additional complications with respect to specifying r_{thal}, $\eta|_{r_{thal}}$, and c_0 when using the migration rate equation. With the present state of knowledge, these terms cannot be predicted *a priori*; a user would need to develop relationships for these variables as a function of centerline radius (or δ) using either a detailed numerical model such as that in Section 4 or obtaining field data to develop reasonable relationships. The complication is that the numerical model of Section 4 is mechanistic and requires no arbitrary parameters but is not free of requiring calibration. The Mackinaw River application showed that applying the field grain size distribution yields unrealistic results in terms of the cross-sectional shape. Effectively, a calibration process was required in Section 5 in which D_{50} was increased to make the numerical results reasonably represent the field data. This suggests the mechanistic numerical model is lacking important processes or is poorly characterizing those processes it simulates. Sufficient analyses have not been performed to indicate whether the good calibration result obtained was simply fortunate or is more generally

applicable. Regardless, the model obviously and intentionally neglects important physical factors, with implications for applying the results. Almost innumerable factors could be cited that were neglected which may be important in certain circumstances, but several major factors stand out as warranting elaboration: (a) the hydrodynamic treatment; (b) sediment sorting and stratification; (c) and the mechanics of the cohesive top layer.

First, the hydrodynamic treatment assumed a hydrostatic pressure distribution in the vertical, which neglects the effects of vertical accelerations that are likely important close to the bank. Transverse and vertical transport of downstream momentum were neglected, and the radial component of momentum was not explicitly solved. Such simplifications were necessary to obtain boundary shear stress distributions quickly due to the large number of time steps required to achieve the steady-state migration. Applying a more sophisticated three-dimensional nonhydrostatic hydrodynamic model with the boundary shape obtained by the simplified model would be worthwhile to ascertain whether the $\boldsymbol{\tau_b}$ distribution (both magnitude and direction) in the near-bank region is realistic or warrants substantial improvement. A further hydrodynamic issue is that form drag was not accounted; if form drag was significant, the $\boldsymbol{\tau_b}$ associated with skin friction that drives sediment motion would be reduced. Decreasing $\boldsymbol{\tau_b}$ to account for form drag has the same effect on migration rate as artificially increasing τ_{c0} as was done in Section 5, decreasing the excess shear stress term. Secondly, given the fining upward grain size distribution observed in both the banks and the point bar at the field site, the issue of sorting and stratigraphy (e.g., Parker & Andrews, 1985) is clearly significant in determining the shape of both bar and banks. The present model assumes a single grain size; it takes no account of different τ_{c0} and transport deviation angles of sediment grains based on grain size. The concentration of large diameter grains at the base of the bank common in bends may limit the transverse component of bed material transport across the thalweg, thus slowing the migration rate due to the reduced demand for bank material. Focusing strictly on the bank, in addition to the modified τ_{c0} and transport deviation angles associated with grain size, the structure of the bank material is also not incorporated into the model. The banks at the field site were not comprised of loose, unstructured deposits as assumed in the model; they were structured deposits with interlocked grains that certainly influences τ_{c0} and θ_{rp} (Millar & Quick, 1993). Third, the effect of the cohesive top layer on bank migration processes is significant when it comprises a large percentage of the bank height, as in the Mackinaw River. Mass failure of the material yields slump blocks that influence

τ_{c0} of the lower bank and mitigates migration rates (e.g., Parker et al., 2011). The current analysis has made no attempt to decipher the relative effects of these and other complicating factors, but for the Mackinaw River case, the analysis strongly suggests that additional factors are playing a significant role in determining cross-sectional shape and migration rate than that included in the simplified model. Whether the sum of these unaccounted effects can be reasonably represented for application on most rivers by increasing D_{50} (and consequently τ_{c0}) as in the Mackinaw River case requires further exploration.

Finally, application of the modeling approach developed in Section 4 outside the framework of a lumped bank erosion model in a high-resolution cross-section-based model such as BSTEM or CONCEPTS is beyond the scope of the present analysis. However, a few obvious considerations warrant highlighting. A morphologically active flow below the top of the noncohesive layer will generate an interface on the bank that separates a lower region subject to fluvial erosion, and an inactive upper region. In such an event, oversteepening and shallow planar mass failures would be expected within the noncohesive layer, and such a process would need to be incorporated into such a model. The mechanics of the upper cohesive layer, including both fluvial erosion and mass failure, would also need to be explicitly incorporated.

Acknowledgments

This work was funded by the Illinois Water Resources Center (Grant: Streambank Erosion in the Mackinaw River, Illinois) when the first author was a graduate student at University of Illinois at Urbana-Champaign. Thanks are extended to the following: Gary Parker and Davide Motta for many helpful discussions during the analysis; Zhenduo Zhu and Dimitrios Fytanidis for assistance with field work; Don Rollo, the property owner, for cooperation with field work and allowing access to the site.

Appendix A

The volume of bed material sized sediment eroded per unit length of centerline in the region $r > r_{thal}$ is defined as $\forall_e$; the volume deposited in the region $r \leq r_{thal}$ is defined as $\forall_d$. For steady-state migration to be possible, $\forall_e$ must equal $\forall_d$ within each unit of time. The volumetric erosion and deposition rates are expressed in Eqs. (A1) and (A2), respectively; each equation contains an

exact and an approximate form, in which the latter are the solutions of the integrals based on an assumed linear relationship between η and r.

$$\frac{\partial \Psi_e}{\partial t} = \int_{\eta|_{r_{thal}}}^{\eta|_{r_{out}}} (1-\lambda) M \frac{r}{r_c} dz \approx M\left(\eta|_{r_{out}} - \eta|_{r_{thal}}\right)(1-\lambda)\frac{(r_{out}+r_{thal})/2}{r_c} \quad \text{(A1)}$$

$$\frac{\partial \Psi_d}{\partial t} = \int_{\eta|_{r_{thal}}}^{\eta|_{r_{in}}} (1-\lambda) M \frac{r}{r_c} dz \approx M\left(\eta|_{r_{in}} - \eta|_{r_{thal}}\right)(1-\lambda)\frac{(r_{thal}+r_{in})/2}{r_c} \quad \text{(A2)}$$

The equivalence between Eqs. (A1) and (A2) in their exact form is expressed in Eq. (A3):

$$\left(\int_{\eta|_{r_{thal}}}^{\eta|_{r_{out}}} r dz\right)\Big|_{r>r_{thal}} = \left(\int_{\eta|_{r_{thal}}}^{\eta|_{r_{in}}} r dz\right)\Big|_{r\leq r_{thal}} \quad \text{(A3)}$$

Eq. (A3) is based on the problem definition that M and r_c are constant, along with an assumption of constant λ. The functional relationship between η and r is not known *a priori*; but regardless of this relationship, the r values are uniformly larger in the left-hand-side than the right-hand-side of Eq. (A3). This requires that $\eta|_{r_{out}}$ must be less than $\eta|_{r_{in}}$ to achieve the equivalence since the lower limits of the integral are equal. This is demonstrated more intuitively using the approximate form of Eqs. (A1) and (A2). Equating the erosion rates and deposition rates yields:

$$\frac{(r_{thal}+r_{in})}{(r_{thal}+r_{out})} \approx \frac{\left(\eta|_{r_{out}} - \eta|_{r_{thal}}\right)}{\left(\eta|_{r_{in}} - \eta|_{r_{thal}}\right)} \quad \text{(A4)}$$

In Eq. (A4), the left-hand-side is necessarily less than unity, which consequently requires that $\eta|_{r_{out}}$ be less than $\eta|_{r_{in}}$. For the numerical analysis of Section 5, the most physically reasonable value of $\eta|_{r_{out}}$ is the maximum value of $\eta|_{r_{in}}$ at which sediment can be transported and deposited, assuming that the outer bank is a previously formed inner bend lateral accretion deposit. However, Eqs. (A3) and (A4) indicate a steady-state solution does not exist for $\eta|_{r_{out}} = \eta|_{r_{in}}$. If $\eta|_{r_{out}}$ is established too high on the bank, then more volume is eroded outside the thalweg than can be deposited inside the thalweg as the steady-state geometry is approached. The result is that the channel continually aggrades until no portion of the channel cross section is competent to transport sediment ($M = 0$), which is not a viable equilibrium geometry if the stream has any bed material sediment load. These considerations constrain the elevation of $\eta|_{r_{out}}$ since it must be less

than $\eta|_{r_{in}}$, while $\eta|_{r_{in}}$ has a physical limit based on the maximum elevation at which bankfull flow is competent to transport sediment.

The approach used herein to calculate $\eta|_{r_{out}}$ is an approximation based on Eq. (A4) that is primarily intended to establish $\eta|_{r_{out}}$ consistently over a range of conditions rather than suggesting a rigorous value of $\eta|_{r_{out}}$ based on physical principles. The variables r_{thal}, $\eta|_{r_{thal}}$, and $\eta|_{r_{in}}$ in Eq. (A4) are not known *a priori*; in fact, the first two are key variables being sought in the numerical solution. The first of these terms is approximated as $r_{thal} = r_{out}$, and the left-hand-side of Eq. (A4) then simplifies to $r_c/(r_c + B/2)$. The second term, $\eta|_{r_{thal}}$, is anticipated to be somewhat deeper relative to the floodplain surface than the reference channel depth (H_0) due to scour at the outside of the bend; however, the possibility exists that under certain conditions, the numerical simulation may yield a very wide, shallow channel. The simplest approximation to allow for either deepening or shallowing relative to the reference condition is to set $\eta|_{r_{thal}} = -H_0$, in which the floodplain surface serves as the vertical datum. The above approximations are expressed in Eqs. (A5) and (A6).

$$r_{thal} \approx r_{out} = r_c + \frac{B}{2} \tag{A5}$$

$$\eta|_{r_{thal}} \approx -H_0 \tag{A6}$$

The third unknown term in Eq. (A4), $\eta|_{r_{in}}$, can be approximated more realistically. Assuming the dominant hydrodynamic forces are associated with the downstream components of gravity and bed shear stress, the maximum possible elevation of $\eta|_{r_{in}}$ at which sediment can be transported and deposited is approximated as follows:

$$\tau^*|_{r_{in}} = \tau^*_{c0} \tag{A7}$$

$$\tau^*|_{r_{in}} \approx \frac{h|_{r_{in}} S|_{r_{in}}}{R_s D_{50}} = \frac{h|_{r_{in}} S_c r_c}{R_s D_{50} r_{in}} \tag{A8}$$

$$\eta|_{r_{in}} \approx -h|_{r_{in}} \tag{A9}$$

Combining Eqs. (A7) through (A9) yields:

$$\eta|_{r_{in}} \approx -\tau^*_{c0} \frac{R_s D_{50} r_{in}}{S_c r_c} \tag{A10}$$

Substituting Eqs. (A5), (A6), and (A10) into Eq. (A4) yields:

$$\eta|_{r_{out}} = -H_0 + \left(\frac{r_c}{r_c+\frac{B}{2}}\right)\left(H_0 - \tau^*_{c0} \frac{R_s D_{50} r_{in}}{S_c r_c}\right) \tag{A11}$$

in which the floodplain surface is the vertical datum. Equation (A11) yields reasonable values for $\eta|_{r_{out}}$ with viable steady-state migration for most conditions evaluated, but values were slightly too high on the bank to prevent aggradation to a static channel for all conditions. Noting that Eq. (A8) may overestimate $\tau^*|_{r_{in}}$ due to momentum extraction at the side boundary not accounted for in the equation and that a transverse slope may warrant a somewhat greater value than τ^*_{c0} in Eq. (A7), a coefficient was added to the right-hand-side of Eq. (A8). Through trial and error, the coefficient 1.2 yielded a steady-state solution over all the evaluated conditions. The modified version of Eq. (A11) used to set $\eta|_{r_{out}}$ in the simulations is thus:

$$\eta|_{r_{out}} = -H_0 + \left(\frac{r_c}{r_c+\frac{B}{2}}\right)\left(H_0 - 1.2\tau^*_{c0} \frac{R_s D_{50} r_{in}}{S_c r_c}\right) \tag{A12}$$

Appendix B: Details of Hydrodynamic Treatment

The velocity vector is represented by three components *u*, *v*, *w*, which represent the streamwise, radial, and vertical components, respectively. In the near-bank region where the *w* component of velocity is non-negligible, a three-dimensional hydrodynamic model accounting for non-hydrostatic pressure would clearly be the most accurate treatment; however, it comes at a significant computational expense. Most morphodynamics models use depth-averaged hydrodynamics, with the assumption of hydrostatic pressure. In the modified cylindrical coordinates for steady, uniform bend flow with hydrostatic pressure assumption, the mass and momentum (*s* and *r*) conservation equations before depth-averaging are as follows:

$$\frac{1}{r}\frac{\partial(\mathrm{v}r)}{\partial r} + \frac{\partial w}{\partial z} = 0 \tag{B1}$$

$$-g\frac{\partial \xi}{\partial s} + \frac{\partial}{\partial r}\left(\frac{(\nu_T+\nu)}{r}\frac{\partial(ur)}{\partial r}\right) + \frac{\partial}{\partial z}\left((\nu_T+\nu)\frac{\partial u}{\partial z}\right) - \mathrm{v}\frac{\partial u}{\partial r} - w\frac{\partial u}{\partial z} - \frac{u\mathrm{v}}{r} = 0 \tag{B2}$$

$$-g\frac{\partial \xi}{\partial r}+\frac{\partial}{\partial r}\left(\frac{(\nu_T+\nu)}{r}\frac{\partial(\mathrm{v}r)}{\partial r}\right)+\frac{\partial}{\partial z}\left((\nu_T+\nu)\frac{\partial \mathrm{v}}{\partial z}\right)-\mathrm{v}\frac{\partial \mathrm{v}}{\partial r}-w\frac{\partial \mathrm{v}}{\partial z}+\frac{u^2}{r}=0 \quad \text{(B3)}$$

where g is the gravitational acceleration constant; ν_T is the turbulent eddy viscosity; and ν is the molecular kinematic viscosity of water. The w momentum equation, not shown, simplifies to a linear relation between pressure and depth below the free surface.

Treatment of the r-momentum equation, Eq. (B3), is based on van Bendegom (1947) and Rozovskii (1961) as described in Jansen et al. (1979; Ch. 2.2.8 therein). Such analyses are based on fully-developed bend flow in the region away from the bank, which allows usage of the hydrostatic pressure assumption and neglecting all terms in Eq. (B3) except the following: the first term (pressure gradient), the second term (r- shear on z- faces), and the last term (centripetal acceleration). In the near-bank region, where v and w will be of the same order of magnitude, the error introduced through this simplification must be considered significant; however, in the present state of knowledge, a tractable method to integrate the equations to yield suitably simple formulations for use in morphodynamics models does not exist.

References

Abad, J. D., & García, M. H. (2006). RVR Meander: A toolbox for re-meandering of channelized streams. *Computers & Geosciences*, 32(1), 92-101.

Ariathurai, C. R. (1974). *A finite element model for sediment transport in estuaries,* (Doctoral dissertation). University of California, Davis.

Asahi, K., Shimizu, Y., Nelson, J., & Parker, G. (2013). Numerical simulation of river meandering with self-evolving banks. *Journal of Geophysical Research: Earth Surface*, 118(4), 2208-2229.

Blanckaert, K. (2011). Hydrodynamic processes in sharp meander bends and their morphological implications. *Journal of Geophysical Research: Earth Surface*, 116(F1).

Brooks, N. H., & Shukry, A. (1963). Discussion of "Boundary Shear Stresses in Curved Trapezoidal Channels". *Journal of the Hydraulics Division*, 89(3), 327-345.

Darby, S. E., Rinaldi, M., & Dapporto, S. (2007). Coupled simulations of fluvial erosion and mass wasting for cohesive river banks. *Journal of Geophysical Research: Earth Surface*, 112(F3).

1216 Diplas, P. (1990). Characteristics of self-formed straight channels. *Journal of Hydraulic*
1217 *Engineering*, 116(5), 707-728.
1218 Duan, J. G., & Julien, P. Y. (2005). Numerical simulation of the inception of channel
1219 meandering. *Earth Surface Processes and Landforms*, 30(9), 1093-1110.
1220 Duan, J. G., Wang, S. S., & Jia, Y. (2001). The applications of the enhanced CCHE2D model to
1221 study the alluvial channel migration processes. *Journal of Hydraulic Research*, 39(5), 469-
1222 480.
1223 Engelund, F. (1974). Flow and bed topography in channel bends. *Journal of the Hydraulics*
1224 *Division*, 100(11), 1631-1648.
1225 Eke, E., Parker, G., & Shimizu, Y. (2014). Numerical modeling of erosional and depositional
1226 bank processes in migrating river bends with self-formed width: Morphodynamics of bar
1227 push and bank pull. *Journal of Geophysical Research: Earth Surface*, 119(7), 1455-1483.
1228 Fernandez Luque, R., & Van Beek, R. (1976). Erosion and transport of bed-load sediment.
1229 Journal of hydraulic research, 14(2), 127-144.
1230 Friedkin, J. F. (1945). *A laboratory study of the meandering of alluvial rivers*. U.S. Waterways
1231 Experiment Station, Vicksburg, MS.
1232 Glover, R. E., & Florey, Q. L. (1951). *Stable Channel Profiles* (Hydraulics Laboratory Report
1233 no. 325). Denver, CO: U.S. Bureau of Reclamation.
1234 Gough, S. C. (1994). *Geomorphic reconnaissance and draft management strategy for the*
1235 *Mackinaw River ecosystem, Illinois*. The Nature Conservancy, Peoria, Illinois Field Office.
1236 Hackney, C., Best, J., Leyland, J., Darby, S. E., Parsons, D., Aalto, R., & Nicholas, A. (2015).
1237 Modulation of outer bank erosion by slump blocks: Disentangling the protective and
1238 destructive role of failed material on the three-dimensional flow structure. *Geophysical*
1239 *Research Letters*, 42(24), 10-663.
1240 Hasegawa, K. (1989). Universal bank erosion coefficient for meandering rivers. *Journal of*
1241 *Hydraulic Engineering*, 115(6), 744-765.
1242 Ikeda, S. (1981). Self-formed straight channels in sandy beds. *Journal of the Hydraulics*
1243 *Division*, 107(4), 389-406.
1244 Ikeda, S., & Nishimura, T. (1986). Flow and bed profile in meandering sand-silt rivers. *Journal*
1245 *of Hydraulic Engineering*, 112(7), 562-579.

1246 Ikeda, S., Parker, G., & Sawai, K. (1981). Bend theory of river meanders. Part 1. Linear
1247 development. *Journal of Fluid Mechanics*, 112, 363-377.
1248 Ikeda, S., Parker, G., & Kimura, Y. (1988). Stable width and depth of straight gravel rivers with
1249 heterogeneous bed materials. *Water Resources Research*, 24(5), 713-722.
1250 Jansen, P., Van Bendegom, L., Van den Berg, J., De Vries, M., & Zanen, A. (1979). *Principles*
1251 *of river engineering: the non-tidal alluvial river*. Pitman Publishing, London.
1252 Johnstone, P. D. (2003). Surficial geology of Tazewell County, Illinois. *Open File Series 2003-*
1253 *06a.* Illinois State Geological Survey, Champaign, Illinois.
1254 Khodashenas, S. R., & Paquier, A. (1999). A geometrical method for computing the distribution
1255 of boundary shear stress across irregular straight open channels. *Journal of Hydraulic*
1256 *Research*, 37(3), 381-388.
1257 Kikkawa, H., Ikeda, S. & Kitagawa, A. (1976). Flow and bed topography in curved open
1258 channels. *Journal of the Hydraulics Division*, 102(9), 1327-1342.
1259 Klavon, K., Fox, G., Guertault, L., Langendoen, E., Enlow, H., Miller, R., & Khanal, A. (2017).
1260 Evaluating a process-based model for use in streambank stabilization: Insights on the Bank
1261 Stability and Toe Erosion Model (BSTEM). *Earth Surface Processes and Landforms*, 42(1),
1262 191-213.
1263 Kovacs, A., & Parker, G. (1994). A new vectorial bedload formulation and its application to the
1264 time evolution of straight river channels. *Journal of Fluid Mechanics*, 267, 153-183.
1265 Lane, E. W. (1955). Design of stable channels. *Transactions of the American Society of Civil*
1266 *Engineers*, 120(1), 1234-1260.
1267 Langendoen, E. J., & Simon, A. (2008). Modeling the evolution of incised streams. II:
1268 Streambank erosion. *Journal of Hydraulic Engineering*, 134(7), 905-915.
1269 Langendoen, E. J., Mendoza, A., Abad, J. D., Tassi, P., Wang, D., Ata, R., et al. (2016).
1270 Improved numerical modeling of morphodynamics of rivers with steep banks. *Advances in*
1271 *Water Resources*, 93, 4-14.
1272 Mackin, J. H. (1948). Concept of the graded river. *Geological Society of America Bulletin*, 59(5),
1273 463-512.
1274 McAnally, W. H., & Mehta, A. J. (2001). Preface. In W. H. McAnally & A. J. Mehta (Eds.),
1275 *Coastal and estuarine fine sediment processes, Proceedings in Marine Science* (Vol. 3, pp. v-
1276 vii). Amsterdam: Elsevier.

1277 Millar, R. G., & Quick, M. C. (1993). Effect of bank stability on geometry of gravel rivers.
1278 *Journal of Hydraulic Engineering*, 119(12), 1343-1363.
1279 Mosselman, E. (1998). Morphological modelling of rivers with erodible banks. *Hydrological*
1280 *Processes*, 12(8), 1357-1370.
1281 Motta, D., Abad, J. D., Langendoen, E. J., & García, M. H. (2012). A simplified 2D model for
1282 meander migration with physically-based bank evolution. *Geomorphology*, 163, 10-25.
1283 Motta, D., Langendoen, E. J., Abad, J. D., & García, M. H. (2014). Modification of meander
1284 migration by bank failures. *Journal of Geophysical Research: Earth Surface*, 119(5), 1026-
1285 1042.
1286 Nanson, G. C. (1980). Point bar and floodplain formation of the meandering Beatton River,
1287 northeastern British Columbia, Canada. *Sedimentology*, 27(1), 3-29.
1288 Osman, A. M., & Thorne, C. R. (1988). Riverbank stability analysis. I: Theory. *Journal of*
1289 *Hydraulic Engineering*, 114(2), 134-150.
1290 Parker, G. (1978). Self-formed straight rivers with equilibrium banks and mobile bed, Part 2, The
1291 gravel river. *Journal of Fluid Mechanics*, 89(1), 127-146.
1292 Parker, G. (1984). Discussion of "Lateral bed load transport on side slopes" by Syunsuke Ikeda
1293 (November, 1982). *Journal of Hydraulic Engineering*, 110(2), 197-199.
1294 Parker, G., & Andrews, E. D. (1985). Sorting of bed load sediment by flow in meander bends.
1295 *Water Resources Research*, 21(9), 1361-1373.
1296 Parker, G., Shimizu, Y., Wilkerson, G. V., Eke, E. C., Abad, J. D., Lauer, J. W., et al. (2011). A
1297 new framework for modeling the migration of meandering rivers. *Earth Surface Processes*
1298 *and Landforms*, 36(1), 70-86.
1299 Pizzuto, J. E. (1990). Numerical simulation of gravel river widening. *Water Resources Research*,
1300 26(9), 1971-1980.
1301 Rinaldi, M., & Darby, S. E. (2008). Modelling river-bank-erosion processes and mass failure
1302 mechanisms: Progress towards fully coupled simulations. In H. Habersack, H. Piegay, M.
1303 Rinaldi (Eds.), *Gravel-Bed Rivers VI: From Process Understanding to River Restoration* (pp.
1304 213-239). Amsterdam: Elsevier.
1305 Rinaldi, M., & Nardi, L. (2013). Modeling interactions between riverbank hydrology and mass
1306 failures. *Journal of Hydrologic Engineering*, 18(10), 1231-1240.

1307 Rinaldi, M., Mengoni, B., Luppi, L., Darby, S. E., & Mosselman, E. (2008). Numerical
1308 simulation of hydrodynamics and bank erosion in a river bend. *Water Resources Research*,
1309 44(9).
1310 Rozovskii, I. L. (1961). *Flow of water in bends of open channels*: Israel Program for Scientific
1311 Translation. Jerusalem, 233p.
1312 Schumm, S. A., & Khan, H. R. (1972). Experimental study of channel patterns. *Geological*
1313 *Society of America Bulletin*, 83(6), 1755-1770.
1314 Seminara, G., Solari, L., & Parker, G. (2002). Bed load at low Shields stress on arbitrarily
1315 sloping beds: Failure of the Bagnold hypothesis. *Water Resources Research*, 38(11), 31-1.
1316 Shimizu, Y., Takebayashi, H., Inoue, T., Hamaki, M., Iwasaki, T., & Nabi, M. (2014). *Nays2DH*
1317 *Solver Manual*. iRIC Project, Hokkaido, Japan.
1318 Simon, A., Curini, A., Darby, S. E., & Langendoen, E. J. (2000). Bank and near-bank processes
1319 in an incised channel. *Geomorphology*, 35(3-4), 193-217.
1320 Siviglia, A., & Crosato, A. (2016). Numerical modelling of river morphodynamics: Latest
1321 developments and remaining challenges. *Advances in Water Resources*, 93(Part A), 1-3.
1322 Stecca, G., Measures, R., & Hicks, D. M. (2017). A framework for the analysis of noncohesive
1323 bank erosion algorithms in morphodynamic modeling. *Water Resources Research*, 53(8),
1324 6663-6686.
1325 Thorne, C. R. (1982). Processes and mechanisms of river bank erosion. In R. D. Hey, J. C.
1326 Bathurst, C. R. Thorne (Eds.), *Gravel-bed Rivers* (pp. 227–271). Chichester: Wiley.
1327 Thorne, C. R., & Tovey, N. K. (1981). Stability of composite river banks. *Earth Surface*
1328 *Processes and Landforms*, 6(5), 469-484.
1329 Thorne, C. R., Alonso, C., Borah, D., Darby, S., Diplas, P., Julien, P., et al. (1998). River width
1330 adjustment. I: Processes and mechanisms. *Journal of Hydraulic Engineering*, 124(9), 881-
1331 902.
1332 Tsujimoto, T. (1999). Fluvial processes in streams with vegetation. *Journal of Hydraulic*
1333 *Research*, 37(6), 789-803.
1334 van Bendegom, L. (1947). Some considerations on river morphology and river improvement. *De*
1335 *Ingenieur*, 59(4), 1-11 (in Dutch; English transl.: Nat. Res. Counc. Canada, Technical
1336 Translation 1054, 1963).

1337 Vanoni, V. A., (Ed.). (1975). *Sedimentation Engineering*, ASCE Manual and Reports on
1338 Engineering-Practice, 54, New York.
1339 Waterman, D. M. (2017). *Non-cohesive bank migration in meandering rivers and bank accretion*
1340 *in weakly braided rivers* (Doctoral dissertation, University of Illinois at Urbana-Champaign).
1341 Waterman, D. M., & García, M. H. (2016). Concave-upward composite river bank profile shape
1342 at migrating meander bends. In *International Conference on Fluvial Hydraulics, RIVER*
1343 *FLOW 2016* (pp. 1098-1105). CRC Press/Balkema.
1344 Waterman, D. M., & García, M. H. (2019). Nonlinear Bedload Transport Trajectory Angle
1345 Expressed in a Traditional Form: Derivation and Application. *Journal of Hydraulic*
1346 *Engineering*, 145(8), 04019028.
1347 Wiberg, P. L., & Smith, J. D. (1987). Calculations of the critical shear stress for motion of
1348 uniform and heterogeneous sediments. *Water Resources Research*, 23(8), 1471-1480.